P-T evolution of metapelites from the Bajgan complex in the Makran accretionary prism, south eastern Iran

Maryam Dorani [a,*], Mohsen Arvin [a], Roland Oberhänsli [b], Sara Dargahi [a]

[a] Department of Geology, Shahid Bahonar University of Kerman, Iran
[b] Institut für Geowissenschaften, Universität Potsdam, Postfach 601553, D-14415 Potsdam, Germany

ARTICLE INFO

ABSTRACT

The Bajgan Complex, one of the basement constituents of the arc massif in Iranian Makran forms a rugged, deeply incised terrain. The complex consists of pelitic schists with minor psammitic and basic schists, calc silicate rocks, amphibolites, marbles, metavolcanosediments, mafic and felsic intrusives as well as ultra-mafic rocks. Metapelitic rocks show an amphibolite facies regional metamorphism and contain garnet, biotite, white mica, quartz, albite $\pm$ rutile $\pm$ apatite. Thermobarometry of garnet schist yields pressure of more than 9 kbar and temperatures between 560 and 675 °C. The geothermal gradient obtained for the peak of regional metamorphism is 19 °C/km, corresponding to a depth of ca. 31 km. Replacement of garnet by chlorite and epidote suggest greenschist facies metamorphism due to a decrease in temperature and pressure through exhumation and retrograde metamorphism (370–450 °C and 3–6 kbar). The metapelitic rocks followed a 'clockwise' P–T path during metamorphism, consistent with thermal decline following tectonic thickening. The formation of medium-pressure metamorphic rocks is related to presence of active subduction of the Neotethys Oceanic lithosphere beneath Eurasia in the Makran.

© 2017 Published by Elsevier GmbH.

1. Introduction

The Iranian plateau which is located in the central part of the Alpine–Himalayan orogenic belt between the Arabian and Eurasian plates, has been divided into several major tectonic units characterized by a diverse structural history and developed through long and complicated plate tectonic processes that started in the Late Proterozoic and ended in Tertiary (Berberian and Berberian, 1981; Berberian and King, 1981; Aghanabati, 1995; Berberian, 2014) (Fig. 1). The three outstanding, NW-SE trending are: (a) the Zagros fold–thrust belt (ZFTB), (b) the Sanandaj-Sirjan zone (SSZ) and (c) the Urmia- Dokhtar Magmatic Assemblage (UDMA) (Fig. 1) which are known as the Zagros orogenic belt of Iran (Förster et al., 1972; Jung et al., 1976; Berberian et al., 1982; Ahmad and Posht Kuhi, 1993; Alavi, 2004). The Zagros orogenic belt and the Iranian plateau preserve a noticeable record of the convergence history between Eurasia and Arabia (~150 ma. to present) which started with a sub-duction/obduction process and ended by the present-day collision between the two plates (Ahmad and Posht Kuhi, 1993).

The northwest-southeast trending SSZ (roughly 200 Km wide) is a part of the Iranian plateau and can be traced from northwest Iran to Makran accretionary prism for about 1600 km. The zone lies between the ZFTB in the south and southwest bordered by a number of strongly dismembered and mylonitized ophiolite assemblages and the UDMA of Central Iran to the northeast. To the northwest, the intracontinental trough of the SSZ is exposed in southeast Turkey. Subduction of the Neotethys Ocean which lied between the Afro-Arabian plate and Iranian micro plates and subsequent continental collision (during Cretaceous to Early Tertiary), resulted in metamorphism and magmatism in the SSZ (Sengör, 1984; Mohajjel et al., 2003; Moazzen et al., 2004). A series of thrust faults in the SSZ are responsible for transporting numerous considerable slivers of Phanerozoic meta-morphosed rocks. Field evidences from stratigraphic column and synorogenic conglomerates indicate that thrusting initiated during Late-Cretaceous (Sarkarinejad et al., 2008). The SSZ is consisted of various Paleozoic and Mesozoic Barrovian-type and Abukuma-type metamorphosed volcano–sedimentary (magmatic arc) rocks together with obducted Paleozoic and Mesozoic ophiolites along the suture lines of collision (Berberian, 1976, 1977, 1983, 1989;
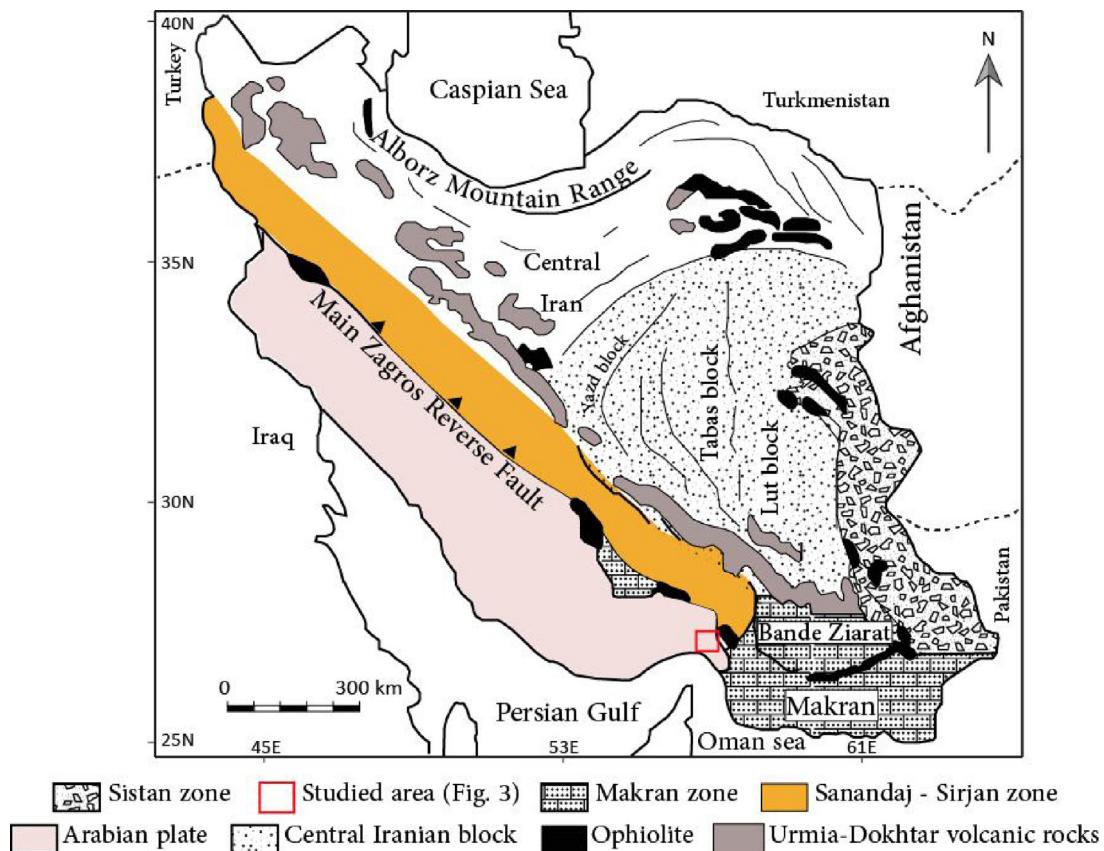
Fig. 1. Simplified structural subdivision map of Iran and the locality of the studied area (modified after Omrani et al., 2013).

Berberian and Alavi-Tehrani, 1977; Berberian and King, 1981; Ghasemi et al., 2002; Berberian, 2014). The SSZ can be traced from northwest Iran through the Makran E–W accretionary wedge in the south east (Berberian, 2014) which is a fragment of the Iranian plateau that formed above the active Makran subduction zone. Along this subduction zone, the Arabian (Oman) seafloor is being subducted beneath the Makran accretionary wedge of south-eastern Central Iran. Subduction probably started during the Palaeocene, leading to an initiation of accretion during the Eocene and the modern accretionary prism since the Late Miocene (Berberian, 2014). The prism has about 6 km of sediments over a low-angle (5°) subduction zone, with a deformation front approximately along the 3000 m depth contour in the north Oman Sea (Jacob and Quittmeyer, 1979; Berberian and King, 1981; McCall and Kidd, 1982; White, 1982; White and Louden, 1982; Palvis and Bruhn, 1983; Harms et al., 1984; McCall, 1985b, 1997, 2003; Platt et al., 1985, 1988; Laane and Chen, 1989; Byrne et al., 1992; Ravaut et al., 1997; Kopp et al., 2000; Hosseini-Barzi and Talbot, 2003; Smith et al., 2013; Berberian, 2014; Omrani et al., 2017).

In the Makran area, the SSZ consists of Early Paleozoic metamorphic basement rocks of the Bajgan Complex (McCall and Kidd, 1982; Davoudzadeh et al., 1986), overlain to the east by a highly disrupted, Lower and Upper Cretaceous continental shelf limestones, from the backstop and remnant rafts of Carboniferous, Permian and Jurassic Dur kan Complex (Fig. 2) (McCall and Kidd, 1982; McCall 1985b, 1997; Hunziker et al., 2015). The Sanandaj-Sirjan/Bajgan-Dur kan Complex is a long but narrow microcontinent that extends from western Makran possibly into the south Armenian block (Oberhänsli, 2016, personal communication) and represents one of a number of microcontinents, which were detached from Gondwana no later than Early Triassic (Stocklin, 1968; Takin, 1972; Haynes and Reynolds, 1980; Ricou, 1994; McCall, 1997; Sengör et al., 1988). This

microcontinent tapers off at its southern end near Band-e-Zeyarat ophiolite and the metamorphic basement disappears, becoming completely buried (Ghazi et al., 2004).

Besides a few short field report about general geology of Bajgan complex (McCall, 1985a) there is no detailed study on the formation of metapelitic rocks in the Bajgan complex. The aim of this paper is to integrate the data from metamorphic textures and mineral chemistry data to unravel the metamorphic process (s) of these rocks. Phase diagram analysis and P–T grids are used to study the sequence of mineral assemblages, estimate metamorphic P–T conditions and define the P–T paths experienced by the pelitic rocks in the Bajgan complex. We hope that the results of this study could shed some light on the tectonic evolution of Makran region and as a whole subduction of Neotethys Ocean.

2. Geological setting

The Iranian Makran is about 350 km wide and located between the Jaz Murian Depression and the Gulf of Oman coast in southeastern Iran. The area has been subdivided into three geotectonic units: (1) Cenozoic main Makran accretionary prism, (2) Mesozoic developments of ophiolite sequences, and (3) two microcontinental blocks; Bajgan-Dur-kan and Deydar (Fig. 2) (McCall, 1997, 2002, 2003). The Cenozoic Makran accretionary prism were divided into four main sequences: (a) Upper Miocene-Pliocene neritic and coastal sediments, (b) Lower-Upper Miocene neritic sediments, (c) Upper Oligocene-Lower Miocene flysch turbidites and (d) Lower Eocene-Lower Oligocene flysch turbidites (Fig. 2). The Mesozoic ophiolites partly exist as classic ophiolitic mélange of tectonic origin in south of the Bajgan-Dur kan microcontinental block and contains two large bodies of ultramafic rocks named Sorkhband and Rudan. The Sorkhband body is marked with lay-
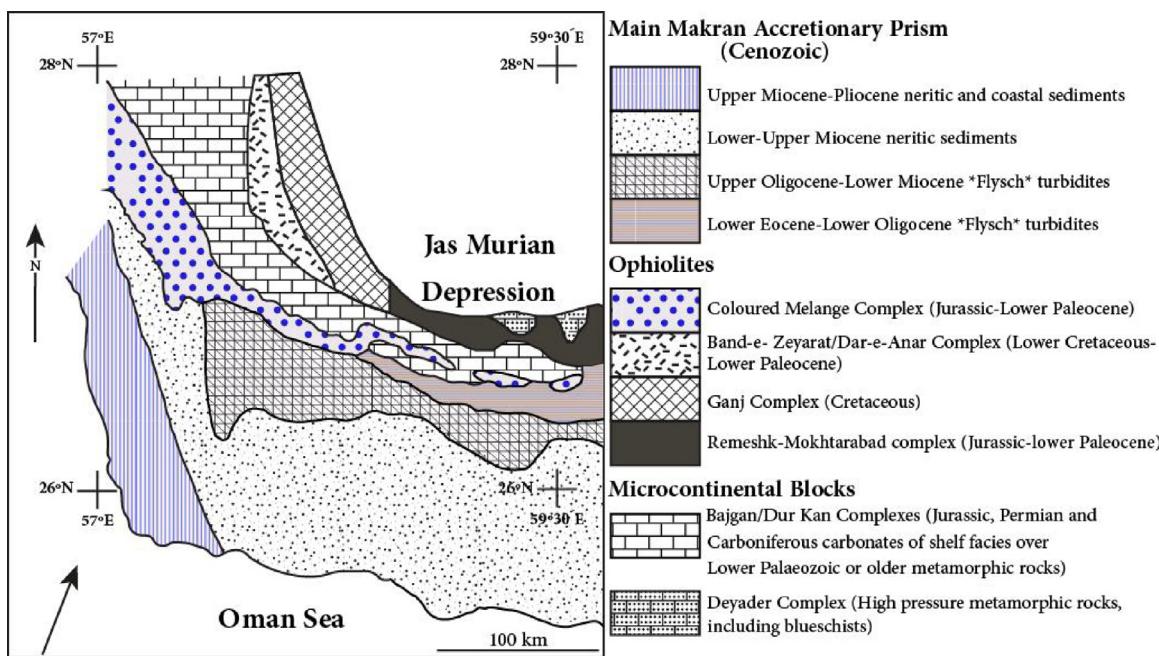
Fig. 2. Generalized geological map of the Makran accretionary prism and the adjacent areas (modified after McCall, 2003). The arrow indicates the present vector of the subduction plate.

ered chromitite and scarce pyroxenite and gabbro while Rudan outcrops are mostly harzburgite (Fig. 3). The Makran ophiolite north east of the Bajgan-Dur kan microcontinental block contains three relatively well preserved complete sequences and are known as Band-e-Zeyarat/Dar-e-Anar, Ganj and Remeshk-Mokhtarabad (Fig. 2). Interlayered with volcanic rocks in the Makran ophiolites are Jurassic to Paleogene deep oceanic sedimentary rocks such as micrite, radiolarite, and Globotruncana limestone (McCall, 1997, 2002, 2003). These ophiolites represent remnants of former narrow oceanic crust (Arvin et al., 2001; Kananian et al., 2001; McCall, 2003; Arvin et al., 2005; Najafzadeh et al., 2008). The two microcontinental blocks together with Mesozoic ophiolites, to the north, are found behind the Cenozoic accretionary prism (Fig. 2). The microcontinental blocks are divided into the Bajgan-Dur kan Complexes and the Deyader metamorphic Complex, lying on Lower Paleozoic or older metamorphic basement rocks (McCall, 2003). The Deyader metamorphic complex is located to the north of Remeshk −Mokhtarabad ophiolites on the southern edge of the Jaz Murian Depression (Fig. 2) and is belived to be the southern tip of the Tabas microcontinental block (Fig. 1) (McCall, 1997, 2003).

The Bajgan Complex (Early Paleozoic or older?) is structurally overlain by Cretaceous Dur kan Complex and is outlined on the Kahnuj and Now Dez geological maps (Fig. 3) (Morgan et al., 1980). To the southeast, the Bajgan Complex dips beneath the Dur kan Complex. The latter is formed by folded Mesozoic sediments including shelf limestones, sandstones, argillites and phyllites, interbedded lavas and small basic intrusions. The Bajgan Complex is separated from the Dar-e-Anar Complex by a major high angle, east dipping, Sabzevaran reverse fault (Fig. 3). East of this fault, 5 km south of Kahnuj, minor outcrops of the Bajgan complex are intruded by gabbros of the Band-e-Zeyarat ophiolitic complex (Fig. 3). To the south of the Bajgan Complex an ophiolitic mélange occurs which mainly comprises of disrupted fragments of various rock types (McCall, 1985a).

Structural features within the Bajgan Complex point to a series of inferred faults that are believed to follow the E-NE trend of Darreh – E-Muri Kardi in the west of Kahnuj (Fig. 3) (Morgan et al., 1980).

North of these inferred faults, schistosity and fold axes of crenulations in the metamorphic rocks trend approximately parallel to the fault (NW-SE) (Figs. 3b, 4a). In the southern part of the Bajgan Complex, the foliation trends N-NW and N-NE in the mapped rocks.

The Bajgan Complex forms a rugged, deeply eroded terrain (Morgan et al., 1980) with a diverse metamorphic rocks suggesting a variety of original rocks and the degree of metamorphism, Pelitic schists (Fig. 4b) with minor psammitic, basic schists, calc silicate rocks (Fig. 4b, e), amphibolites (Fig. 4c), recrystallized limestones (Fig. 4d), metavolcano sediments (Fig. 4d), as well as basic and acidic intrusive rocks (Fig. 4c), are examples of such diverse lithology. Elongate bodies of metagabbros with minor schist and serpentinite and one body of metadiabase crop out at southeast of Deh Kahan (Fig. 3).

The ultrabasic rocks, believed to be tectonically emplaced, probably during Alpine orogeny (Fig. 4e), contain highly tectonized, anastomosing serpentinite (Fig. 4f) and chromite bodies that concentrated along fault zones (McCall, 1985a). At the north of Deh Kahan village, within the Bajgan Complex, (Fig. 3) a chromite deposit occurs in a serpentinised dunite body (Fig. 3a) (Morgan et al., 1980).

McCall (1985a) defined three zones (A, B and C) of progressive metamorphism in both basic and pelitic schists in the Bajgan Complex, each separated by east- west trending isogrades (Fig. 3b). He inferred, from south to north, moderately high pressure-temperature type of metamorphism from greenschist facies to amphibolite facies. McCall's sudy concluded a moderately high pressure (3–9 kb) and high temperature (350–400C) metamorphism in the A and C zones. Moreover, Morgan et al. (1980) has definied biotite and almandine isogrades based on mineral assemblages in the pelitic rocks (Fig. 3b).

3. Petrography

To better understand the degree of metamorphism of Bajgan Complex, 40 samples of metapelitic rocks were prepared for petrographic analysis and their representative mineral assemblages are
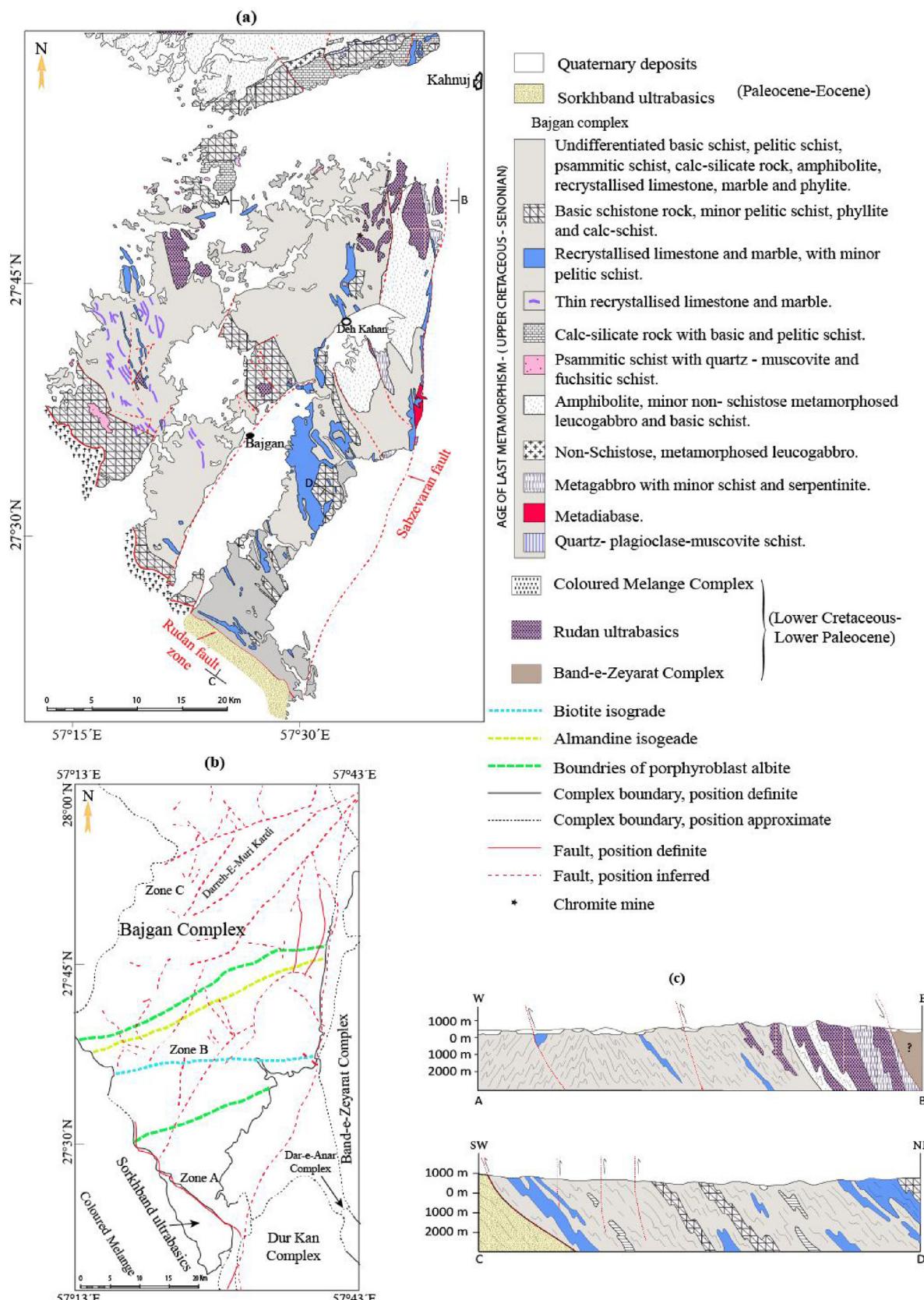
Fig. 3. (**a**) Geological map of the Bajgan Complex (studied area in Fig. 1) showing the main rock types. (**b**) Major structural features, metamorphic zones (after McCall, 1985a) and mineral isogrades accompanied by the boundaries of other adjacent rock units (modified after Morgan et al., 1980). (**c**) Two cross sections from **a**, E-W and NE-SW, illustrating the relation between the main rock units.
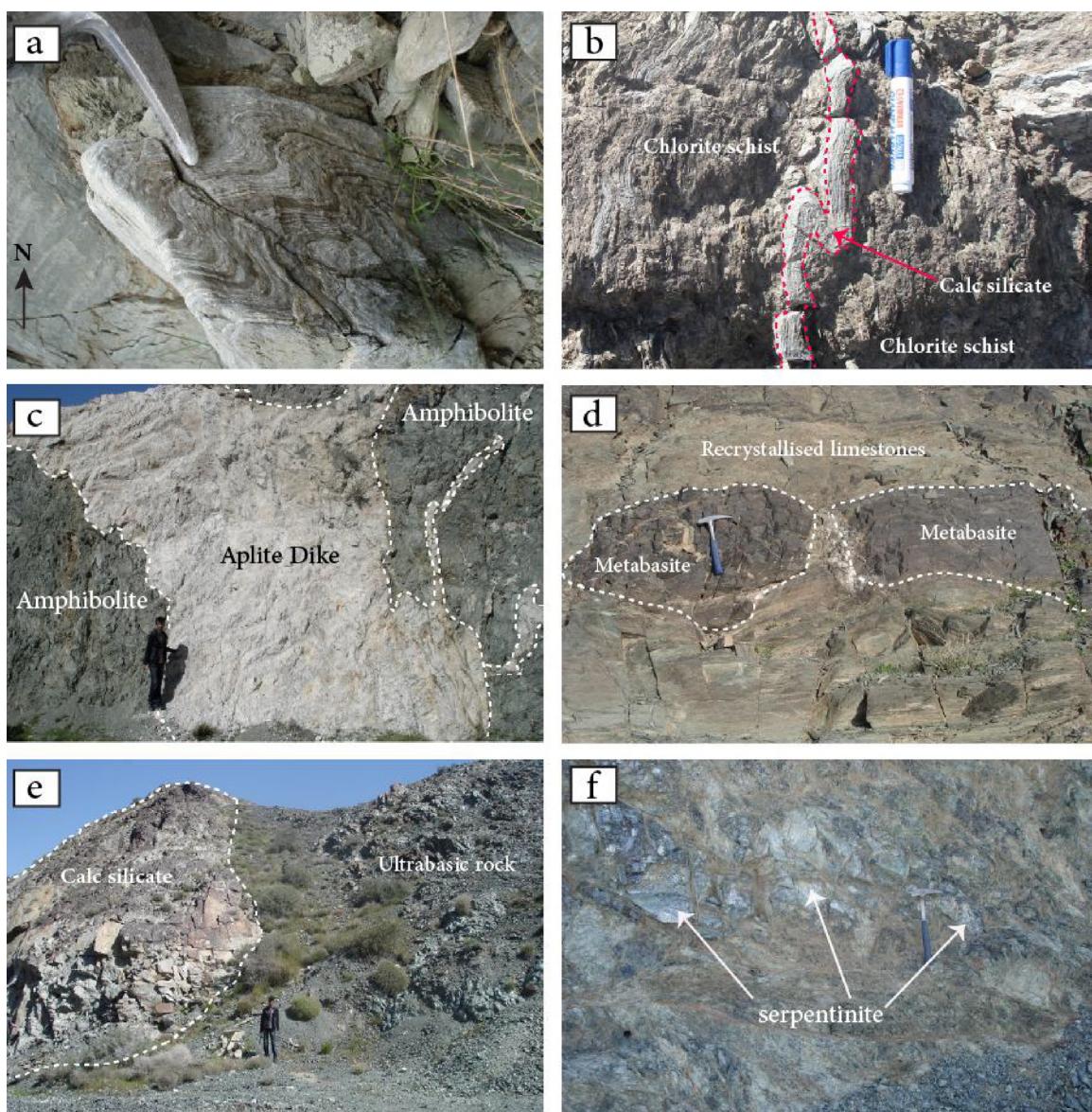
Fig. 4. Some structural and lithologies in the Bajgan Complex: **(a)** NW-SE fold of crenulation in the metamorphic rocks. **(b)** Folded and faulted calc silicate rocks in chlorite schist. **(c)** Aplite dike in amphibolite. **(d)** Amphibole bearing meta-volcanic sediment intercalated with schistose recrystallized limestone. The massive metabasalts occurr along a shear zone in the meta-sediments. **(e)** Sharp contact between calc silicate and ultrabasic rocks. **(f)** Anastomosing serpentinite showing abundant fracturing along the shear zone.

shown in Table 1. A short description of petrography and textural relations of the studied metapelitic rocks is given below.

3.1. Rutile – bearing garnet schist

This rock type occurs locally in the east of the Bajgan Complex and mineralogically consists of garnet + biotite + white mica + quartz + albite ± chlorite ± rutile ± apatite (Fig. 5a). The spaced schistosity is defined by biotite and white mica cleavage domains, showing strong S_1 and a weaker S_2 foliation. In some parts, chlorite as retrograde product from biotite occurs in cleavage domains. Microlithons consist of quartz, albite and garnet. Quartz shows deformation lamellae, undulose extinction, grain boundary migration (GBM) recrystallizations and occasionally appears as grain shape preferred orientation. The presence of myrmekites is a sign of retrograde trend from high to low temperatures (Barker, 1998). Garnet porphyroblasts (0.5 mm in size) have inclusions of quartz, albite, rutile and minor amounts of white mica, biotite and apatite. Fractures of garnets are emplaced by chlorite (Fig. 5a). Albite crystals, 0.7–1 mm in size, are surrounded by biotite and white mica. They show taper twinning, intracrystalline fractures and contain inclusions of biotite and white mica. Occasionally a weak crenulation of biotite and white mica is visible (Fig. 5b) and in some parts, white mica crystals form mica fish. Commonly, trails of small mica fragments extend into the matrix forming the tips of isolated mica fish (Fig. 5c). They are used as reliable shear sense indicators (Passchier and Trouw, 2005). Rutile is seen both in biotite and in the matrix, where garnet was disintegrated. Apatite occurs as inclusions in garnets and rarely in the matrix where they are encircled by biotite and white mica.

3.2. Garnet mica schist

These rocks are mostly found in the southern part of the Bajgan Complex. The mineral assemblage is white mica, biotite, chlorite, garnet, albite, quartz ± titanite ± zircon. White mica and

Table 1
Mineral assemblage and coordinates of the representative metamorphic rocks in the Bajgan complex.

Sample no.	167	168	203	199	268	270	271	125	217
Grt	X	X		O	X	X		X	X
Na-Ca Am				X					
Ca Am				X				X	
Ep group			Xret	O	Xret			Xret	X
Pg	X	X			X	X	X	X	X
Bt	X	X	X		O	O	X		O
Chl	Xret	Xret	Xret		Xret	Xret	X	Xret	Xret
Pl	X	X	O	X	O		O	O	
Rt	Xinc	X	X	O			O	O	
Ttn		O	O	O	O	O		O	
Cal	O	O	O		O	O	O	O	O
Qtz	X	X	X	O	X		X	X	X
Ore	O	O		O				O	O
Ap	Xinc		Xinc					Xinc	
Stp							O		
Coordinate	E560380	E560396	E548872	E548840	E546007	E546011	E546013	E563069	E542340
	N3066029	N3066216	N3082392	N3082446	N3032621	N3032614	N3032613	N3095036	N3067681

X, major mineral; O, minor mineral; X ret, retrograde product; X (inc), inclusion. Mineral abbreviations are after Bucher and Grapes, (2011). **167** Garnet mica schist, **168** Rutile bearing garnet schist, **203** Rutile bearing biotite schist, **199** biotite chlorite schist, **268** Albite garnet chlorite schist, **270** Garnet mica schist, **271** Chlorite mica schist, **125** Epidote-amphibole bearing garnet schist, **217** Garnet epidote schist.

minor amounts of chlorite are the main component of the cleavage domains that form a spaced foliation in these rocks. According to two S_1 and S_2 fabrics (Fig. 5d), they have experienced two deformation phases (D_1 and D_2). The shape of cleavage domains is often wriggly and the spatial relation between cleavage domains shows anastomosing trend. Microlithons are usually rich in quartz, albite and relicts of garnet. Small albite grains (1 mm in size) rarely show taper twinning and contain inclusions of titanite, zircon and minor biotite. Nearly all garnet porphyroblasts (M_1), ∼0.3–0.7 mm in size, are replaced by chlorite (M_2) (Fig. 5e). Recrystallized quartz inclusions show S shape trails in the relicts of garnets, indicating syntectonic crystallization for the garnet. Titanite and zircon are accessory minerals. In some parts, small white micas are surrounded by quartz as a result of GBM recrystallization (pinning, dragging and window microstructure) (Fig. 5f).

3.3. Epidote-amphibole bearing garnet schist

Epidote-amphibole bearing garnet schist is seen in the north of the Bajgan Complex. It comprise of garnet + quartz + phengite + chlorite + albite + amphibole + epidote ± ilmenite ± titanite ± rutile ± apatite. The rock is characterized by a porphyroblastic texture and shows a spaced schistosity defined by amphibole + chlorite + phengite. Syntectonic garnet, ranging between 0.5–0.7 mm in size, has sub-idiomorphic rounded shapes and illustrates crystallization of chlorite after fracturing (Fig. 6a). Inclusions are abundant in garnet and consist of quartz + epidote + zircon + apatite (Fig. 6b). In general, two garnet types are distinguished on the basis of textural relationships. The first type shows an inclusion-poor core overgrown by an inclusion-rich rim (Fig. 6c) whereas the second type consists of inclusions throughout the garnet (Fig. 6d). Recrystallized quartz in the matrix shows undulose extinction, deformation lamellae and Tuttle lamellae (healed microfractures) (Fig. 6e), GBM and BLG (bulging) recrystallizations. Blue-green amphibole, up to 2.5 mm in length, defines the foliation and has brownish rim. Amphibole is partially replaced by chlorite and has inclusions of apatite, epidote and quartz (Fig. 6f). Backscattered electron images reveal that composition of epidote inclusions varies from core to rim as it appears lighter at rims (Fig. 6f). Moreover, epidote (averaging 0.4 mm in diameter) can be found in matrix. The principal Ti minerals in the matrix are titanite, ilmenite and often relicts of rutile (Fig. 6g).

3.4. Biotite- chlorite schist

These rocks crop out at the south of the Bajgan village and consist of white mica + chlorite + biotite + quartz + calcite ± rutile ± stilpnomelane. The two latter minerals are scattered in these rocks. The spaced schistosity (S_1) (a product of the first deformation D_1) is defined by preferred orientation of biotite, white mica and chlorite minerals. Pervasive second deformation (D_2) has clearly affected the S_1 and hence the S_2 foliation can be seen as crenulation cleavage planes. The microfolds show an asymmetric shape and there is a gradual transition between cleavage domains and microlithons. The major components of microlithon are quartz, anhedral and fractured feldspar, calcite and minor amount of white mica and biotite. Biotite is considered as M_1 which defines S_1 and S_2 foliations. As a result of retrograde metamorphism, the chlorite overgrowth (M_2) is visible on biotite (M_1). Quartz shows features of sub grain, undulose extinction, syntaxial overgrowth, BLG and weak GBM (as window microstructure) recrystallizations.

4. Mineral chemistry

Three representative of metapelitic samples (167, 168, and 125) were chosen for microprobe analysis (Tables 1 and 2). Major element compositions of garnet, amphibole, white mica, biotite, plagioclase, chlorite and epidote were obtained by wavelength-dispersive spectrometry using a JEOL 8800 electron microprobe at Potsdam University, Germany. Operating conditions were 15 kV accelerating voltage and 10–20 nA specimen current. The beam diameter was set between 2 and 10 μm. Natural and synthetic standards (rhodonite [Mn], rutile [Ti], wollastonite [Si, Ca], MgO [Mg], orthoclase [Al, k], fluorite [F], albite [Na] and Fe_2O_3 [Fe]) were used for calibration. Representative mineral compositions are given in Table 2.

4.1. Garnet

Garnet occurs in rutile-bearing garnet schist (168), garnet-biotite schist (167) and epidote-amphibole bearing garnet schist (125). In general, all analysed garnets have an almandine-rich solid solution (Fig. 7a, b). Garnet in rutile-bearing garnet schist preserves a growth zoning (Fig. 7d). It is characterized from core to rim by: decreasing grossular content, nearly

Table 2

Representative microprobe analyses for metapelite Epidote –amphibole bearing garnet Schist (125), Rutile-bearing garnet Schist (168) and Biotite-garnet Schist (167) from the Bajgan complex.

Am				Grt							
sample	125				125		168		167		
Type	Ts	Mg-Hbl	Tr								
Note	Core	Rim	Rim		Rim	Core	Core	Rim	Core	Rim	
SiO_2	42.5	51.74	54.1	SiO_2	37.62	38.05	38.27	38.54	37.81	37.87	
TiO_2	0.58	0.06	0.08	TiO_2	0.06	0.12	0.08	0.05	0.08	0.06	
Al_2O_3	14.5	5.11	2.38	Al_2O_3	21.06	21.55	21.62	21.73	21.83	21.77	
FeO	19.1	15.09	14.1	FeO	28.1	25.88	29.72	27.59	29.91	31.05	
MnO	0.40	0.42	0.36	MnO	2.62	4.64	1.73	3.00	0.63	0.37	
MgO	8.50	13.57	15.00	MgO	1.70	0.87	0.96	2.81	1.72	1.60	
CaO	11.5	12.51	12.7	CaO	8.80	9.97	8.65	6.69	8.79	8.21	
Na_2O	1.86	0.71	0.33	Na_2O	0.02	0.06	0.05	0.03	0.00	0.02	
K_2O	0.70	0.19	0.10	K_2O	0.00	0.00	0.01	0.02	0.00	0.00	
Cr_2O_3	0.04	0.01	0.01	Cr_2O_3	0.00	0.04	0.00	0.02	0.03	0.00	
Total	99.6	99.42	99.1	Total	99.99	101.17	101.1	100.5	100.8	100.95	
cations per 23 equivalent Oxygens				*cations per 24 Oxygens*							
T: Si	6.20	7.39	7.70	Si	6.01	6.01	6.07	6.09	5.98	5.99	
Al (IV)	1.80	0.61	0.30	Ti	0.01	0.01	0.01	0.01	0.01	0.01	
Fe^{3+}	0.00	0.00	0.00	Al	3.96	4.01	4.04	4.05	4.07	4.06	
Ti	0.00	0.00	0.00	*Fe^{3+}	0.02	0.00	0.00	0.00	0.00	0.00	
T-Sum	8.00	8.00	8.00	Fe^{2+}	3.74	3.42	3.94	3.65	3.96	4.11	
C: Al (VI)	0.70	0.25	0.10	Mn	0.35	0.62	0.23	0.40	0.08	0.05	
Ti	0.06	0.01	0.01	Mg	0.40	0.21	0.23	0.66	0.41	0.38	
*Fe^{3+}	0.71	0.28	0.20	Ca	1.51	1.69	1.47	1.13	1.49	1.39	
Cr	0.00	0.00	0.00	Na	0.01	0.02	0.01	0.01	0.00	0.01	
Mg	1.85	2.89	3.18	K	0.00	0.00	0.00	0.00	0.00	0.00	
Fe^{+2}	1.62	1.52	1.47	Cr	0.00	0.00	0.00	0.00	0.00	0.00	
Mn	0.05	0.05	0.04	Total	16.00	16.00	16.00	16.00	16.00	16.00	
Ca	0.00	0.00	0.00	Alm(%)	62.25	57.63	67.13	62.41	66.65	69.31	
C-Sum	5.00	5.00	5.00	Prp(%)	6.75	3.46	3.88	11.33	6.83	6.37	
B: Ca	1.79	1.92	1.94	Sps(%)	5.91	10.46	3.96	6.87	1.41	0.84	
Na	0.21	0.08	0.06	Grs (%)	25.09	28.45	25.04	19.38	25.1	23.48	
B-Sum	2.00	2.00	2.00	*XMg	0.10	0.06	0.05	0.15	0.09	0.08	
A: Ca	0.00	0.00	0.00								
Na	0.32	0.11	0.03								
K	0.13	0.03	0.02								
A-Sum	0.45	0.15	0.05								
**X_{Mg}	0.53	0.66	0.68								
Al IV/(AlIV + Fe3 +)	0.5	0.47	0.32								

Phe									Bt						
	125		168			167				168			167		
	in matrix	in Am	in matrix	InGrt	in Pl	InGrt	in Pl	in matrix		InGrt	in Pl	in matrix	InGrt	in matrix	in Pl
SiO_2	49.78	48.55	47.24	46.54	46.51	46.17	46.18	49.52	SiO_2	34.12	34.68	32.61	35.48	34.94	36.18
TiO_2	0.03	0.27	0.36	0.39	0.42	0.37	0.48	0.51	TiO_2	1.75	1.67	1.52	0.60	1.34	1.30
Al_2O_3	28.61	30.44	34.44	36.02	35.63	37.87	34.73	31.88	Al_2O_3	19.72	20.34	19.62	19.59	18.67	19.30
FeO	3.91	3.67	1.76	1.26	0.86	1.29	1.50	1.40	FeO	19.47	18.13	19.74	19.65	19.36	17.64
MnO	0.05	0.03	0.00	0.01	0.00	0.01	0.00	0.01	MnO	0.18	0.18	0.21	0.19	0.20	0.19
MgO	3.22	2.42	1.19	0.96	1.01	0.50	1.81	2.16	MgO	10.76	10.71	11.96	11.03	11.74	11.25
CaO	0.01	0.06	0.01	0.00	0.01	0.00	0.03	0.00	Cr_2O_3	0.05	0.03	0.06	0.04	0.04	0.02
K_2O	10.9	11.07	10.86	10.42	10.37	10.19	10.59	10.75	CaO	0.19	0.13	0.28	0.17	0.25	0.20
Na_2O	0.21	0.18	0.41	0.73	0.67	0.87	0.45	0.36	K_2O	0.15	0.08	0.13	0.11	0.13	0.11
Cr_2O_3	0.00	0.00	0.02	0.01	0.02	0.03	0.03	0.02	Na_2O	7.26	7.79	5.22	7.64	6.44	7.68
Total	96.71	96.67	96.27	96.33	95.51	97.28	95.8	96.63	Total	93.64	93.75	91.35	94.49	93.09	93.85
Tetrahedral site			*cations per 11 equivalent Oxygens*						*cations per 11 equivalent Oxygens*						
Si	3.31	3.23	3.12	3.06	3.08	3.00	3.07	3.25	Si	2.62	2.64	2.55	2.70	2.68	2.74
Al^{IV}	0.69	0.77	0.88	0.94	0.92	1.00	0.93	0.75	Ti	0.10	0.10	0.09	0.03	0.08	0.07
Sum	4.00	4.00	4.00	4.00	4.00	4.00	4.00	4.00	Al^{IV}	1.38	1.36	1.45	1.30	1.32	1.26
Octahedral site									Al^{VI}	0.40	0.47	0.36	0.45	0.37	0.46
Ti	0.00	0.01	0.02	0.02	0.02	0.02	0.02	0.03	Fe	1.25	1.16	1.29	1.25	1.24	1.12
Al^{VI}	1.55	1.62	1.80	1.85	1.86	1.91	1.78	1.71	Mn	0.01	0.01	0.01	0.01	0.01	0.01
Fe	0.22	0.20	0.10	0.07	0.05	0.07	0.08	0.08	Mg	1.23	1.22	1.40	1.25	1.34	1.27
Mn	0.00	0.00	0.00	0.00	0.00	0.00	0.00	0.00	Cr	0.00	0.00	0.00	0.00	0.00	0.00
Mg	0.32	0.24	0.12	0.09	0.10	0.05	0.18	0.21	Ca	0.02	0.01	0.02	0.01	0.02	0.02
Cr	0.00	0.00	0.00	0.00	0.00	0.00	0.00	0.00	K	0.02	0.01	0.02	0.02	0.02	0.02
Sum	2.09	2.07	12.24	2.03	2.03	2.05	2.06	2.03	Na	0.71	0.76	0.52	0.74	0.63	0.74
interlayer									Total	7.75	7.73	7.72	7.77	7.72	7.71
Ca	0.00	0.00	0.00	0.00	0.00	0.00	0.00	0.00	Fe/(Fe + Mg)	0.50	0.49	0.48	0.50	0.48	0.47
K	0.92	0.94	0.92	0.87	0.88	0.85	0.90	0.90	Mg/(Mg + Fe)	0.50	0.51	0.52	0.50	0.52	0.53
Na	0.03	0.02	0.05	0.09	0.09	0.11	0.06	0.05							
Sum	0.95	0.96	0.97	0.96	0.97	0.96	0.96	0.95							
Total	7.04	7.04	7.00	7.01	6.99	7.00	7.03	6.97							
Na/(Na + K)	0.03	0.02	0.05	0.10	0.09	0.11	0.06	0.05							
Mg/(Mg + Fe)	0.60	0.54	0.55	0.58	0.68	0.41	0.68	0.73							
Ms	0.97	0.98	0.95	0.90	0.91	0.89	0.94	0.95							
Pg	0.03	0.02	0.05	0.10	0.09	0.11	0.06	0.05							

Table 2 (*Continued*)

Chl	125 ret.f. Grt	ret.f. Am	168 ret.f. Grt	ret.f. Bt	167 ret.f. Grt	ret.f. Bt	Ep	125	168	Pl	125	168	167
SiO_2	27.64	28.36	27.64	27.40	29.25	29.55	SiO_2	38.46	35.19	SiO_2	69.16	63.92	64.49
TiO_2	0.04	0.04	0.51	0.44	0.16	0.43	TiO_2	0.20	0.20	TiO_2	0.00	0.00	0.00
Al_2O_3	19.40	17.95	19.78	19.55	18.85	19.26	Al_2O_3	26.29	23.75	Al_2O_3	20.17	23.47	22.13
Cr_2O_3	0.01	0.00	0.01	0.04	0.04	0.03	FeO	8.96	9.84	FeO	0.01	0.03	0.02
FeO	27.13	28.47	24.20	24.63	26.10	22.28	MnO	0.19	0.56	MnO	0.03	0.00	0.00
MnO	0.51	0.44	0.27	0.31	0.36	0.30	MgO	0.04	0.08	MgO	0.00	0.00	0.02
MgO	15.51	14.65	15.80	15.89	13.62	15.32	Cr_2O_3	0.03	0.00	Cr_2O_3	0.02	0.01	0.00
CaO	0.13	0.05	0.21	0.25	0.17	0.13	CaO	23.52	18.45	CaO	0.02	3.68	3.02
Na_2O	0.02	0.00	0.00	0.00	0.05	0.05	Na_2O	0.00	0.00	Na_2O	10.89	8.95	9.85
K_2O	0.01	0.03	0.40	0.28	0.79	1.66	K_2O	0.00	0.00	K_2O	0.07	0.12	0.16
Total	90.40	89.99	88.81	88.79	89.38	89.01	Total	97.70	88.07	Total	100.38	100.18	99.70
cations per 14 equivalent Oxygens							*cations per 12.5 equivalent Oxygens*			*cations per 8 equivalent Oxygens*			
Si	2.84	2.95	2.86	2.84	3.03	3.02	Si	3.00	3.03	Si	3.03	2.83	2.85
Ti	0.00	0.00	0.04	0.03	0.01	0.03	Ti	0.01	0.01	Ti	0.00	0.00	0.00
Al	2.35	2.20	2.41	2.39	2.30	2.32	Al	2.41	2.41	Al	1.04	1.22	1.15
Cr	0.00	0.00	0.00	0.00	0.00	0.00	Fe^{3+}	0.58	0.71	Fe^{3+}	0.00	0.00	0.00
Fe^{2+}	2.33	2.48	2.09	2.14	2.26	1.91	Mn	0.01	0.04	Mn	0.00	0.00	0.00
Mn	0.04	0.04	0.02	0.03	0.03	0.03	Mg	0.00	0.01	Mg	0.00	0.00	0.00
Mg	2.38	2.27	2.43	2.46	2.10	2.34	Cr	0.00	0.00	Cr	0.00	0.00	0.00
Ca	0.01	0.01	0.02	0.03	0.02	0.01	Ca	1.96	1.70	Ca	0.00	0.17	0.14
Na	0.00	0.00	0.00	0.00	0.01	0.01	Na	0.00	0.00	Na	0.92	0.77	0.84
K	0.00	0.00	0.05	0.04	0.10	0.22	K	0.00	0.00	K	0.00	0.01	0.01
Total	9.98	9.95	9.93	9.95	9.87	9.89	Total	7.99	7.90	Sum	5.00	5.00	5.00
							XPs	0.19	0.23	An	0.10	18.38	14.37
										Ab	99.51	80.92	84.71
										Or	0.39	0.70	0.92

*$Fe^{3+}$was estimated by charge balance; **$X_{Mg} = Mg/Mg + Fe^{2+}$. **Am** amphibole,**Ts** tschermakite, **Mg-Hbl**magnesiohornblende, **Tr** tremolite, **Grt**garnet. **Phe** phengite,**Bt** Biotite. **Chl** Chlorite, **Ep** Epidote, **Pl** plagioclase, **ret.f. Grt** retrograde from garnet, **ret.f. Am** retrograde from amphibole, **ret.f. Bt** retrograde from biotite.

constant pyrope content, increasing the almandine component from core to mantle and then decreasing towards the rim. In regard to almandine, the spessartine component shows a reverse trend (Fig. 7d). Three representative compositions are: $Alm_{51-52}Grs_{26-27}Sps_{16-17}Prp_{3-4}$ (core), $Alm_{65-68}Grs_{22-25}Sps_{1.5-3}Prp_{5-10}$ (mantle), and $Alm_{62-63}Grs_{15-21}Sps_{5-10}Prp_{9-11}$(rim). A chemical profile across garnets in the epidote-amphibole-garnet schist (Fig. 7c) shows insignificant pyrope increase towards the rim coupled to grossular decrease. Almandine first sharply increases and then decreases towards the rim (Fig. 7c), whereas spessartine first exhibits a noticeable decreasing and then increasing from core to rims. It is characterized by a core composition with $Alm_{50-52}Grs_{30-31}Sps_{14-16}Prp_{2-3}$ a mantle with $Alm_{61-64}Grs_{25-27}Sps_{6-7}Prp_{4-5}$ and a rim with $Alm_{55-60}Grs_{25-26}Sps_{9-14}Prp_{6-6.5}$.

4.2. Amphibole

The analyzed amphiboles of sample 125 show calcic compositions in the nomenclature scheme of Hawthorne et al. (2012). The predominant cations of T and C sites are Si and Mg, respectively and concentration of Al (as Al^{IV}) is on the T site. Although most Na occupies the A site, the content of K and Na on the A site is very low. The site is virtually empty (($(K + Na)_A ≤ 0.31$). There is a compositional change from core to rim as tschermakite, magnesio-hornblende and tremolite (Fig. 8a). This change is associated to increasing X_{Mg} (core 0.04; rim 0.70), Ca (core 1.23; rim 1.94), Si (core 6.17; rim 7.71), and decreasing Na (0.00–0.24a.p.f.u.), Al (0.40–2.59a.p.f.u.), Fe_{total} (1.67–2.40a.p.f.u.) and A-site occupancy (23.39% −2.35%) (Table 2). Note that the Si content of Ca-amphibole increases progressively with decreasing temperature (Ernest and Liu, 1998). All amphiboles in Ca^{tot}/Na^{tot} diagram (Fig. 8b) plot parallel to the Ca–Na exchange vector and indicate an edenite substitution. Fig. 8c, shows aluminium and titanium contents of amphibole that heir concentrations (in high-temperature calcic amphiboles) are pressure and temperature dependent, respectively (Ernest and Liu, 1998). It is apparent that the Ti content of amphibole decreases with decreasing temperature during growth.

4.3. White mica

Representative analyses of phengite have been calculated to 11(O) assuming all iron to be Fe^{2+}. All data of phengite from samples 125, 168 and 167 are plotted on Si-[Mg/(Fe + Mg)], Si-[Na/(Na + K)] and Si-Al diagrams (Fig. 9a–c).The content of silica in phengite is relatively high, ranging between 3.00 and 3.43 c.p.f.u. In the Si versus Al diagram (Fig. 9a–c), the line represents the celadonite substitution. Some analysis plot slightly above the Si (Fe^{2+}, Mg) Al_2 tie line (Fig. 9a, b), suggesting the presence of low amounts of Fe^{3+} (Cetinkaplan et al., 2014) while some plot below the tie line (Fig. 9c), indicating that a part of the Fe is in a trivalent state and it was substituted by Al (López-Carmona et al., 2011), showing significantly high oxidation state in these rocks (Itaya and Fujino, 1999). Variation of X_{Mg} is visible among different samples (Fig. 9a–c) and it is wider in biotite –garnet schist (0.36–0.73 p.f.u.) (Fig. 9a). Tschermakite-substitution ($Mg^{VI}_{-1} Al^{VI}_{+1} Si^{IV}_{-1} Al^{IV}_{+1}$) is visible on a Si–[Mg/(Fe + Mg)] diagram (Fig. 9). All phengites show very low Na content, reaching the maximum 0.10 (p.f.u.) in rutile-bearing garnet schists (Fig. 9b). The ratio of Na/(Na + K) is 0.05 in epidote-amphibole bearing garnet schists (Fig. 9c) and up to 0.12 in rutile-bearing garnet schists (Fig. 9b).

In some parts, phengite in the matrix is distinctly different in composition from the ones included in garnet and plagioclase (Fig. 9a–c). The former shows a wider chemical variation than the latter. This large chemical variation of matrix phengite is due to significant retrograde chemical reactions during the cooling and exhumation of the host schists (e.g. Itaya and Fujino, 1999; Miyashita and Itaya, 2002; Takeshita et al., 2004). Phengite in rutile-bearing garnet schist shows brighter rims than core (Fig. 9d). This probably reflects higher Fe concentration and correspondingly higher Si substitution (Smart and Wakabayashi, 2009). Compositions of white micas from metapelites are plotted on the
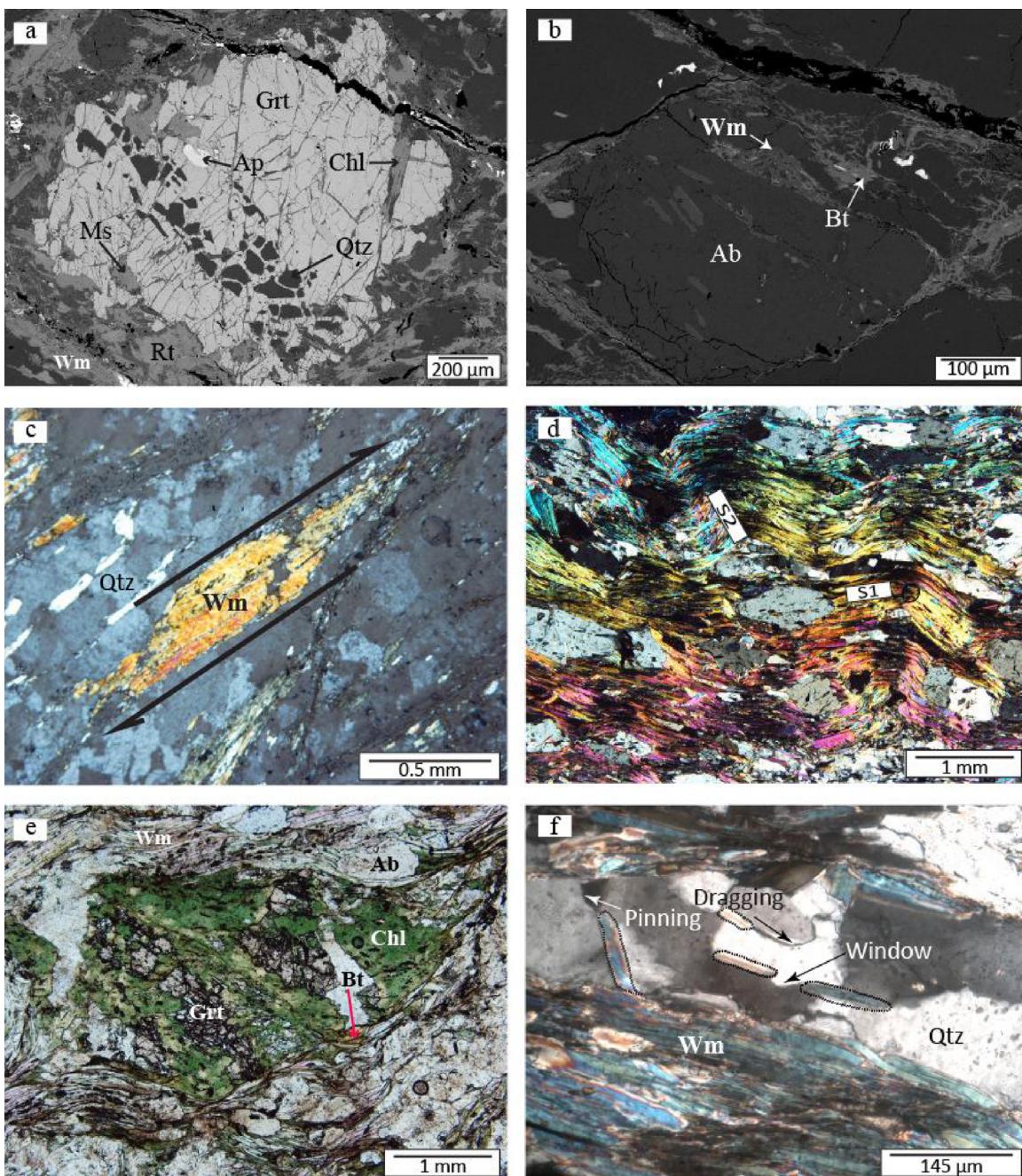
Fig. 5. (**a**) Back-scattered electron image of rutile-bearing garnet schist consisting of garnet, white mica, quartz, albite, chlorite, rutile, apatite. (**b**) Back-scattered electron image of rutile-bearing garnet schist showing inclusions of biotite and white mica in albite. (**c**) In the rutile-bearing garnet schist, the rhomboidal mica fish is visible under crossed polars. Shearing is parallel to long side of the mica fish. (**d**) Under crossed polars, D_1 and D_2 deformational phases in the garnet mica schist manifested by S_1 and S_2 schistosities. (**e**) Photomicrograph, taken in plane-polarized light, showing mineral assemblage of garnet mica schist. Garnet grains are commonly replaced by chlorite. (**f**) Pinning, dragging and window structures of quartz grain boundaries on white mica are shown under crossed polars. Mineral abbreviations are after Bucher et al. (2011).

FeO_T–Al_2O_3 diagram (Fig. 9e) of Miyashiro (1973) where they fall in the field of Chlorite-Biotite-Almandine Zone.

4.4. Biotite

The analyzed biotites of samples 167 and 168 are plotted in a Fe/(Fe + Mg) versus Al^{VI} diagram (Fig. 10a) (Deer et al., 1991). The biotites in the matrix show a wider Al^{VI} variation than those included in garnet and plagioclase (Fig. 10a). The amount of X_{Mg} in biotites varies between 0.44 and 0.52 (p.f.u.) with the highest amounts in biotite-garnet schist (Fig. 10b). In general, Mn concentration is low and shows similar ranges in the two samples

varying between 0.007 and 0.056 (p.f.u.) (Fig. 10b). The Fe/Mg ratio (0.84–1.25) of biotite is variable in both rock types (Fig. 10b). The higher Mg contents of biotite in the matrix compare to biotite in garnet and plagioclase is probably due to higher degree of metamorphism (Deer et al., 1991).

4.5. Chlorite

Assuming no ferric iron and 14 oxygens in the formula, the chlorite compositions of samples 125, 168 and 167 are plotted in Si vs. Mg/(Mg + Fe) diagrams (Fig. 11a) (Hey, 1954). They show compositions which is corresponding to ripidolite, brunsvigite and
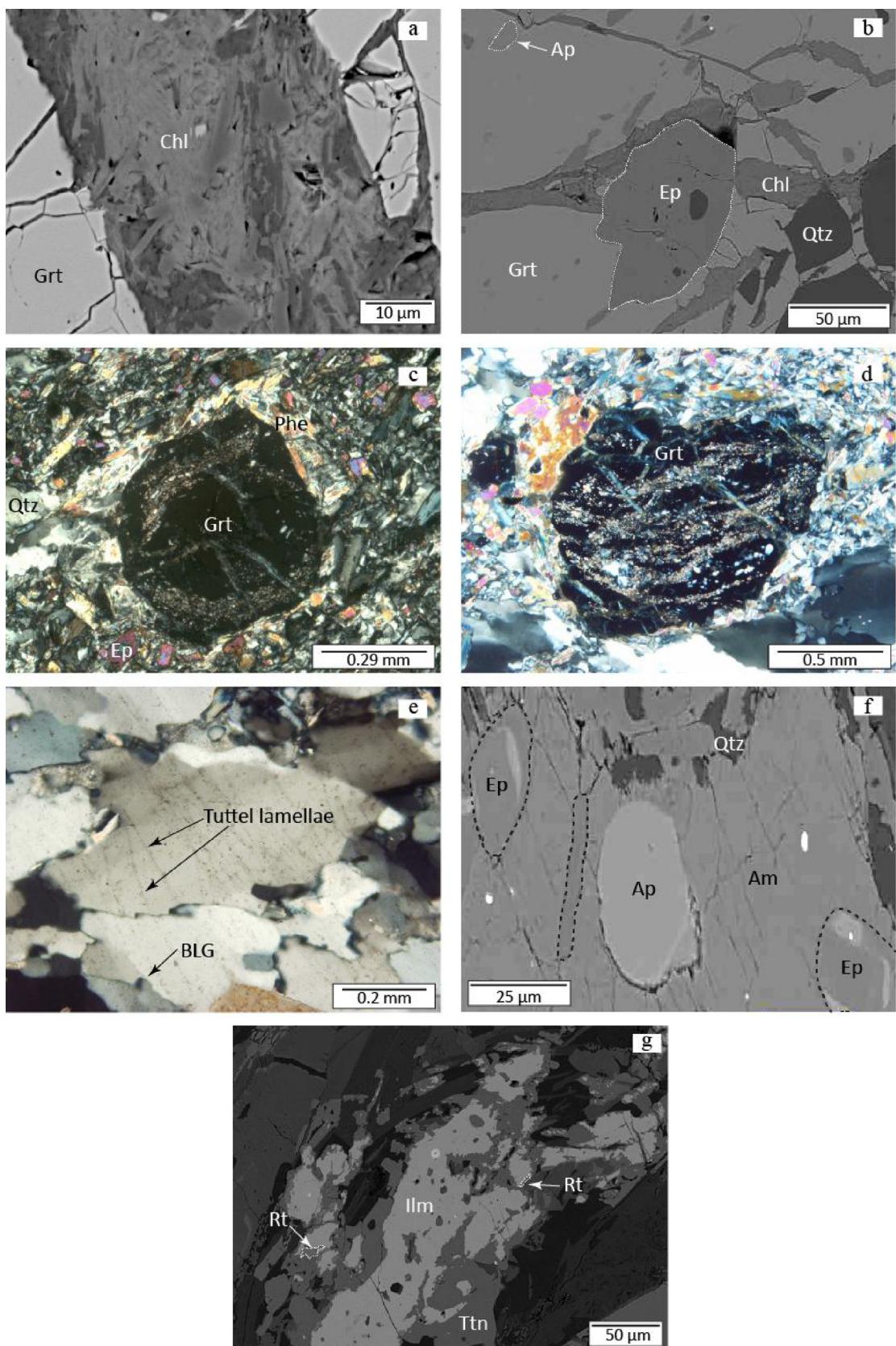
Fig. 6. **(a)** Back-scattered electron image of epidote-amphibole bearing garnet schist showing the replacement by chlorite in the fractures of garnet. **(b)** Back-scatter image showing Qtz, Ep and Ap inclusions in garnet of epidote-amphibole bearing garnet schist. **(c)** Under crossed polars, garnet porphyroblast in epidote-amphibole bearing garnet schist shows the presence of inclusions in rim and lack of those in the core. **(d)** Under crossed polars, syntectonic garnet porphyroblast in epidote-amphibole bearing garnet schist shows curved inclusion pattern throughout the garnet. **(e)** Under crossed polars, tuttle lamellae and BLG recrystallization in quartz of epidote-amphibole bearing garnet schist. **(f)** Qtz, Ep and Ap inclusions and chlorite replacement in amphibole of epidote-amphibole bearing garnet schist. **(g)** Back-scattered electron image of sample 125 illustrates Ti minerals in the matrix. It is worth to note that rare relicts of rutile can be found between ilmenite (core) and titanite (rim).
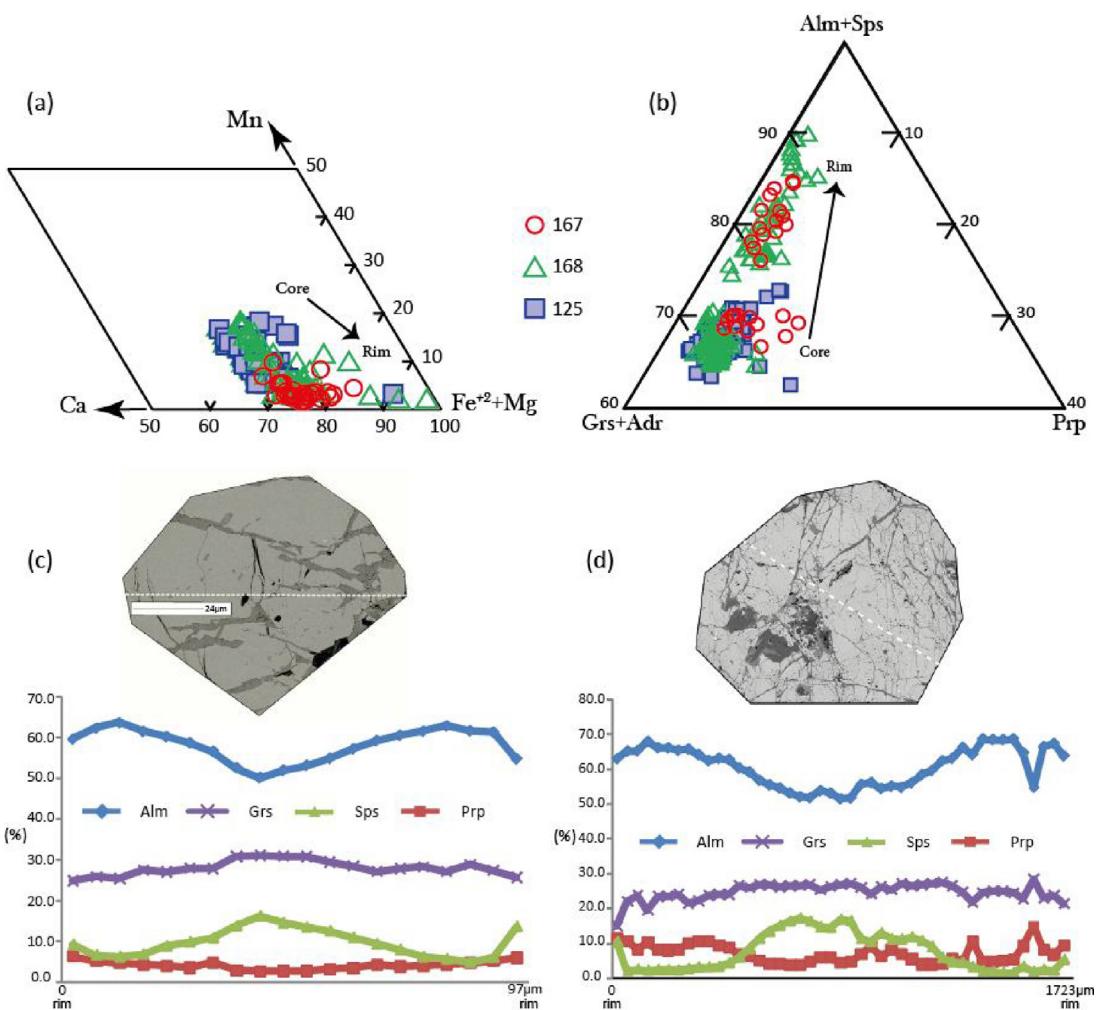
Fig. 7. **(a)** Garnet composition in Ca-Mn-(Fe^{2+} + Mg) and **(b)** Alm + Sps-Grs + Adr-Prp diagrams. Chemical zoning in garnet from **(c)** epidote-amphibole bearing garnet schist (sample 125), **(d)** rutile-bearing garnet schist (sample 168). In the Back-scattered electron images, the dashed lines show microprobe traverse analyses.
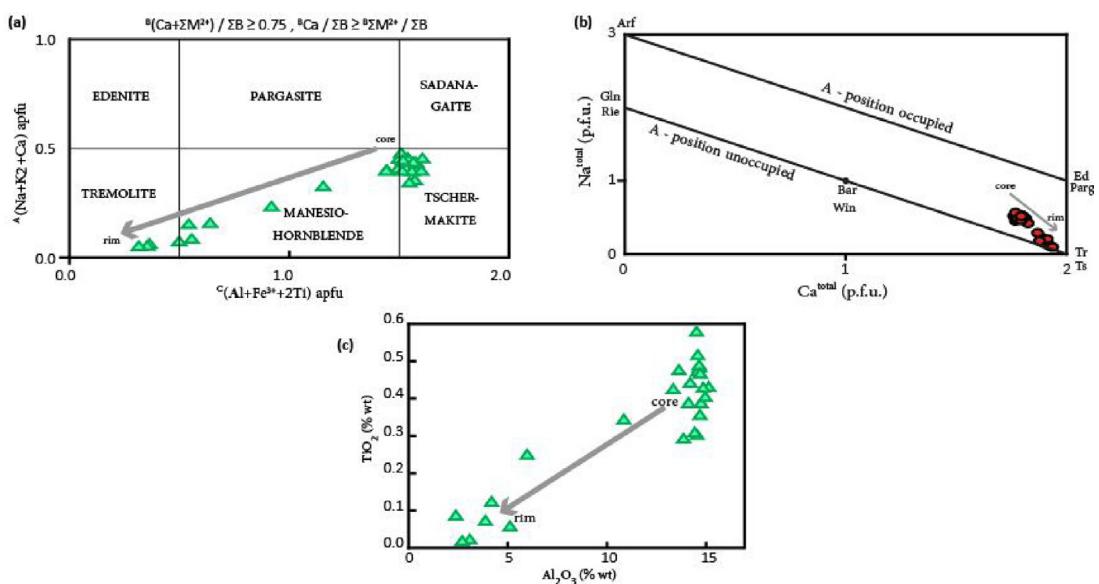
Fig. 8. **(a)** Compositional variations of metapelite's amphiboles in the Bajgan Complex (diagram of Hawthorne et al., 2012). **(b)** Ca$_{total}$ versus Na$_{total}$ diagram (Spear, 1993) to discriminate the Ca–Na exchange vector. **(c)** Aluminium and titanium contents in amphiboles and their variation from core to rim.
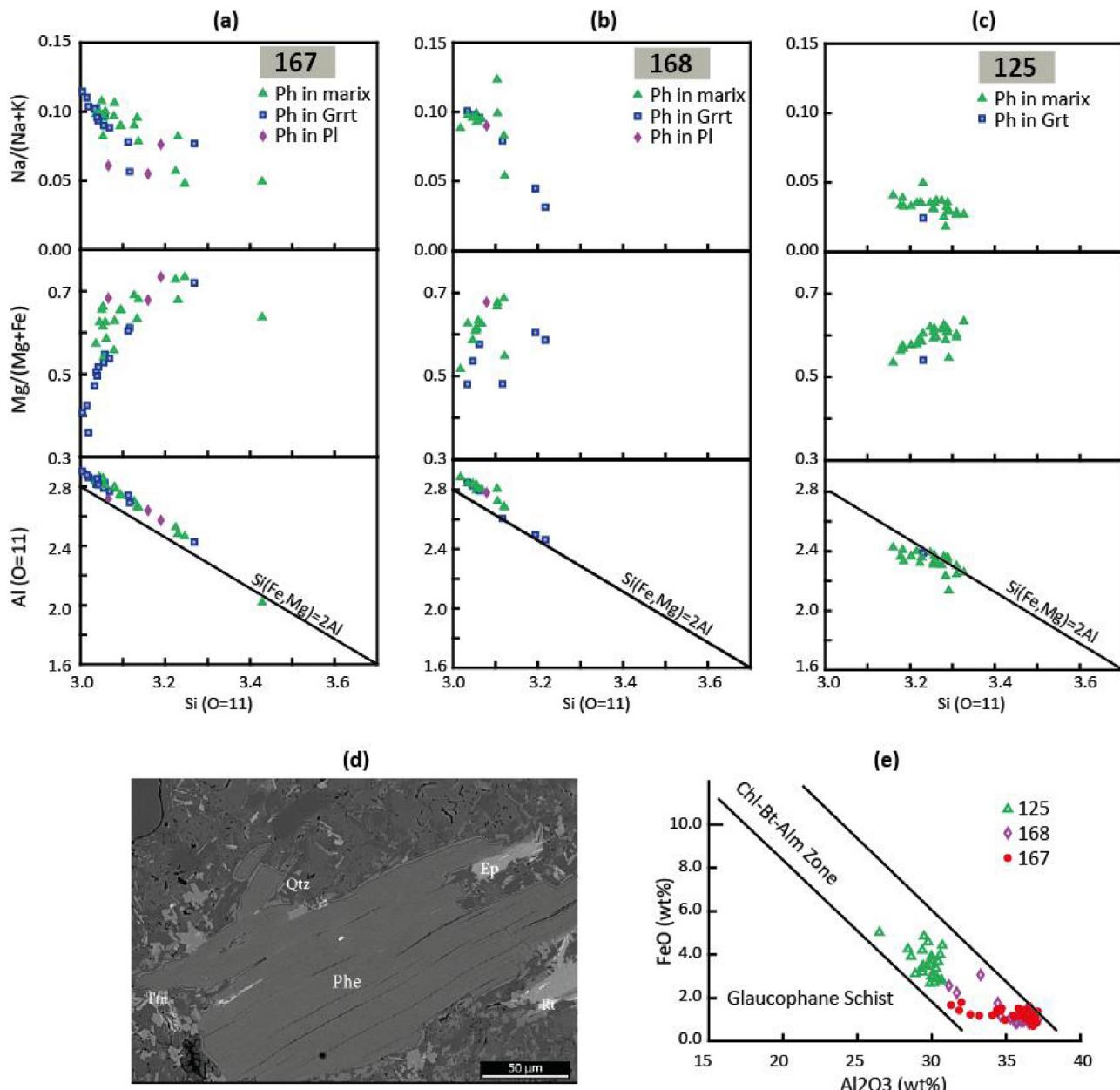
Fig. 9. Phengite compositions plotted in Si versus Na/(Na + K), (Mg/Mg + Fe) and Al diagrams. Line illustrates the ideal celadonite substitution (Si (Fe^{2+}, Mg) Al$_{-2}$) for samples **(a)** 167, **(b)** 168, **(c)** 125. **(d)** Back scattered electron (BSE) image of 168. Phengite (phe), epidote (Ep) titanite (Ttn), rutile (Rt) and quartz (qtz). The rims of the phengites are slightly brighter than the cores, probably reflecting higher Fe concentration and correspondingly higher Si substitution. **(e)** White mica classification diagram based on metamorphic origin (Miyashiro, 1973).

pycnochlorite. From the textural perspective, chlorites are secondary phases replacing garnet, amphibole and biotite (Fig. 11a). In some cases they show distinct chemical compositions. It is possible to distinguish in chlorite a decrease in Fe^{2+} (2.60 to 0.00 a.p.f.u.), with a corresponding increase in Mg (1.66 up to 2.66 a.p.f.u) for different samples (Fig. 11b). Also in chlorite the abundance of Cr and Mn in all samples is ignorable and the highest content of Ti is recorded from sample 168 (0.11 p.f.u.).

4.6. Epidote group minerals

The analyzed epidote group minerals of two samples (125, 168) are classified as clinozoisite subgroup, using nomenclature of Armbruster et al. (2006). The ternary diagram Al-Fe^{3+}-Ca shows that

there is no significant compositional variation in the epidotes from the two samples. Epidote in sample 125 is less ferric than in sample 168. There is a variation of X$_{PS}$ [Ps = pistacite, Fe^{3+}/(Fe^{3+} + Al)] for epidote group minerals founds in the matrix (X$_{PS}$ = 0.19), included in amphibole (X$_{PS}$ = 0.21) and as retrogression product in garnet (X$_{PS}$ = 0.22). A slight compositional zoning was detected in clinozoisites of the matrix where XFe^{3+} shows a weak trend of increasing towards the rim that suggests retrogressive growth with increasing temperature (e.g. Kawai et al., 2008).

4.7. Plagioclase

As illustrated in an An-Ab-Or plot (Fig. 11c), the albite component is dominant in all plagioclases. Plagioclases in sample 125 are
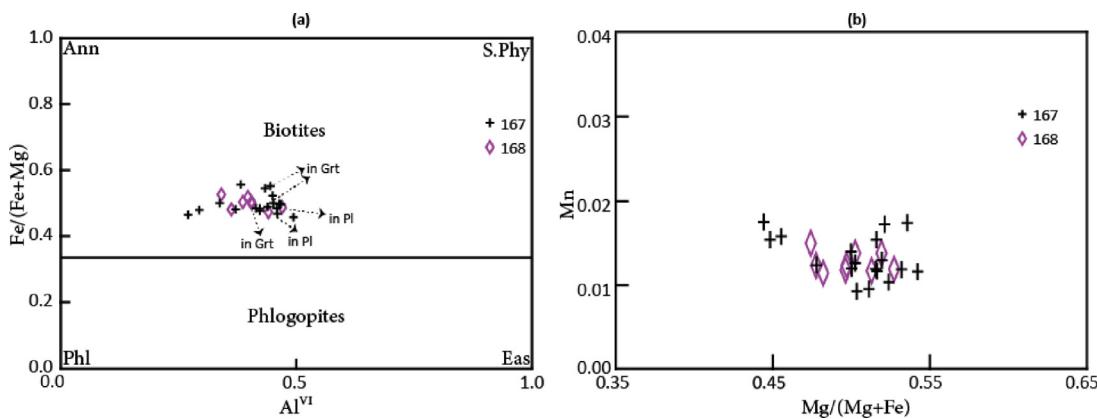
Fig. 10. (a) Phlogopite-biotite compositional fields (Deer et al., 1991). The line indicates Mg:Fe = 2:1. Ann: Annite, S.Phy: Siderophyllite, Phl: phlogopite, Eas: Eastonite. (b) Biotite compositions in Mn versus Mg/(Mg + Fe) diagram.
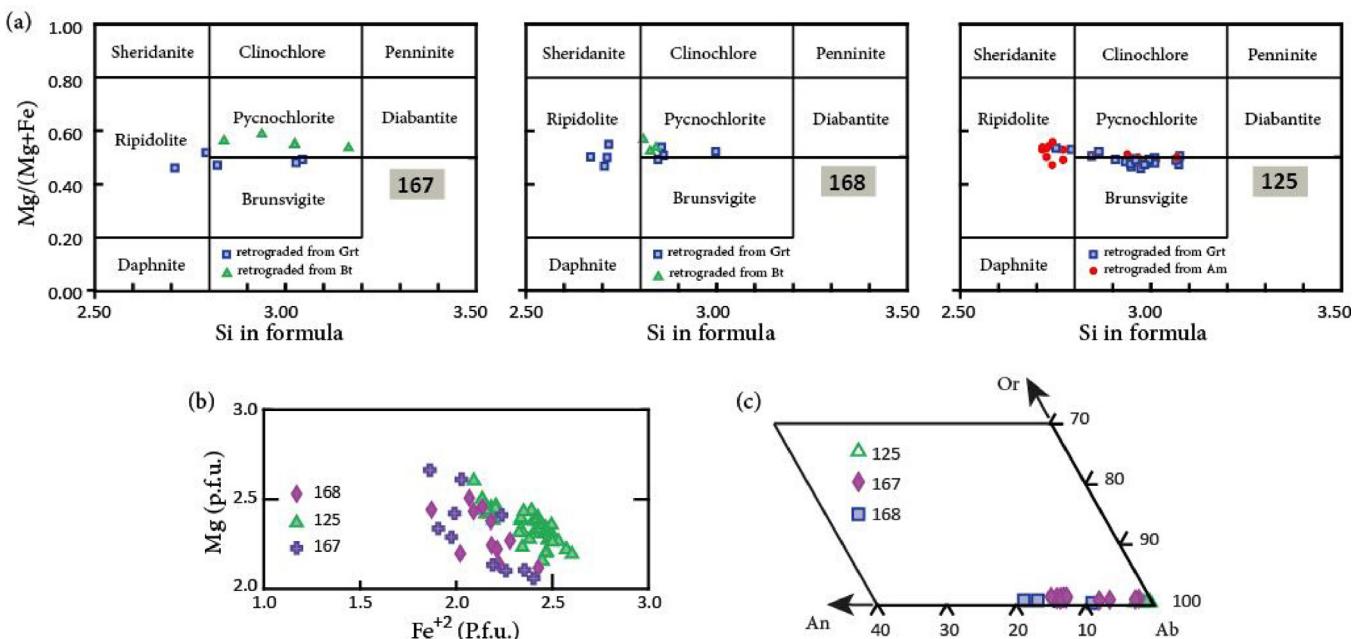
Fig. 11. (a) Chlorite compositions plotted on Si vs. Mg/(Mg + Fe) diagram (all as atoms per formula unit) (Hey 1954). (b) Compositional variations of chlorites in terms of Fe^{2+} (p.f.u.) vs. Mg (p.f.u.)..

nearly pure albite (X_{Ab} = 99.86). The anorthite content (X_{An}) of plagioclases varies between the samples. For example, rutile-bearing garnet schist (X_{An} = 18.4) and garnet-biotite schist (X_{An} = 14.4) have higher anorthite than epidote-amphibole bearing garnet schist (X_{An} = 0.10) and plagioclase has a composition between albite and oligoclase (Fig. 11c). In sample 167, the albite and anorthite content of plagioclase in the matrix and as inclusions in garnet vary from X_{An} = 1.89 and X_{Ab} = 97.5 (in the matrix) to X_{An} = 14.37 and X_{Ab} = 84.71(in the garnet).

5. P–T estimation

Metamorphic conditions for metapelites in the Bajgan Complex are estimated by combining micro-structural observations and two methods of calculations for rutile- bearing garnet schist (sample 168). The first is a conventional method based on local equilibrium and seven calibrations of the garnet–biotite Fe-Mg-exchange. The second method uses Theriak-Domino software (de Capitani and Petrakakis, 2010) based on bulk rock composition to calculate the

pseudosection by using the updated JAN92.RGB thermodynamic database of Berman (1988).

The peak of metamorphism of the metapelitic rocks in the Bajgan Complex is marked by the formation of rutile-bearing garnet schist that contains garnet, biotite, phengite and rutile. Garnet and biotite equilibrium temperatures for rutile-bearing garnet schists were estimated, using seven different geothermometers. In samples where rim compositions of garnet–biotite pairs show textural equilibrium, the metamorphic temperature was estimated between 594 and 610 °C at a given pressure of 9 kbar, using the calibration of Bhattacharya et al. (1992). The temperature range differs when the calibrations of Hodges and Spear (1982); Perchuk and Lavrent'eva (1983); Thompson (1976); Holdaway and Lee (1977); Dasgupta et al. (1991) are used. The range varies from 638 to 663 °C, 574–587 °C, 596–614 °C, 567–584 °C and 633–657 °C, respectively. The temperature of post deformation chlorite crystallization in the garnet fractures was estimated to be ~400 °C, applying the Al^{IV} contents of chlorite calibration of Cathalineau (1988).

The estimated conventional temperature results are consistent with the garnet–albite–biotite–phengite–rutile-quartz stability

Bulk(1)= SI(61.64)AL(18.80)TI(0.63)FE(5.17)MN(0.14)MG(4.03)CA(2.36)NA(4.49)K(2.73)O(166.79)H(60)O(30)
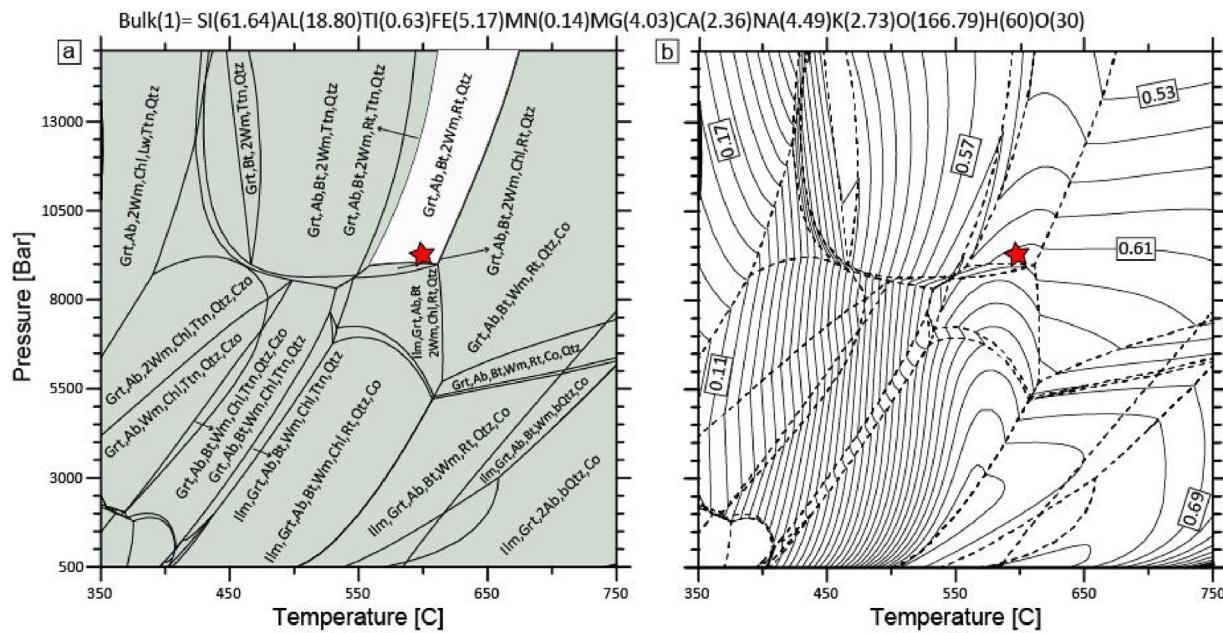
Fig. 12. (a) Pseudosection calculated for sample 168. The light field shows a pressure of 9-15 kbar at temperature of 560–675 °C (stability field). **(b)** The pseudosection in Fig. 12a, which is contoured for the almandine content in garnet, shows a pressure of 9 kbars at a temperature of 600 °C (asterisk in Figs. 14a, b). Calculations with Theriak-Domino (de Capitani and Petrakakis, 2010).
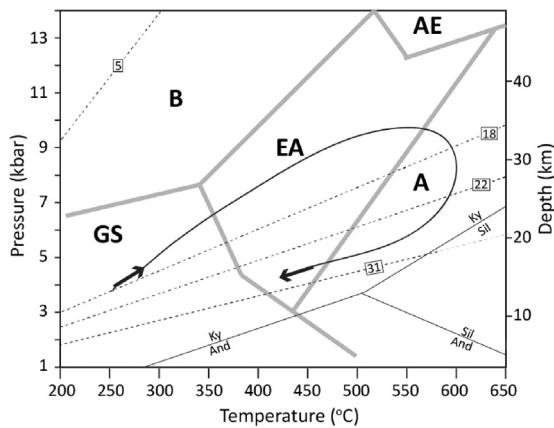
Fig. 13. P–T diagram of rutile-bearing garnet schist. Facies boundaries are after Okamato and Maruyama (1999). AE amphibole- eclogite, B blueschist, A amphibolite, EA epidote-amphibolite, GS greenschist. Dashed lines are simple linear thermal gradients (c°/km).

field calculations by Domino P–T (de Capitani and Petrakakis, 2010) (Fig. 12a). The pseudosection for sample 168 gives pressures higher than 9 kbar and temperatures of 560–675 °C for mineral paragenesis of garnet–albite–biotite–phengite–rutile-quartz. For accurate determination of P-T conditions, the same pseudosection as in Fig. 14a is contoured for the almandine, pyrope and grossular contents in garnet (Fig. 12b). According to our microprobe analysis, the rutile-bearing garnet schist (sample 168) has about 62%, 15% and 21%, of almandine, pyrope and grossular, respectively. The same values of almandine, pyrope and grossular isopleths calculated by Domino intersect at 600 °C 9 kbar. These values can be considered as peak metamorphic temperature and pressure condition, which in turn, can be correlated with an intermediate geothermal gradient of about 19 °C/km (Fig. 13).

Textural studies from chlorite and clinozoisite which replaced garnet, give out temperatures between 370–450 °C and pressures between 3–6 kbar for retrograde conditions. The textural and petrographic evidence indicate that during prograde and subse-

quent retrograde metamorphic cycle, a clockwise P–T loop ensued exhumation of the studied rocks (Fig. 13).

6. Discussion and conclusions

6.1. Prograde metamorphism in the Bajgan complex

The average composition of rutile-bearing garnet schist (sample 168) was used to depict its mineralogical evolution based on P–T increment using Theriak-Domino software (Fig. 14a). During compaction and metamorphism, density and formation water of clays continuously increased and reduced, respectively (Fig. 14b). Minerals underwent significant chemical and mechanical changes during progressive metamorphism (Fig. 14a) as described below.

As it shows in Fig. 14a, muscovite and paragonite mostly coexist and there is a widespread assemblage of muscovite too. As a result of NaK$_{-1}$ exchange, the amount of albite and paragonite simultaneously increase and decrease or vice versa (Bucher and Grapes, 2011).

The first appearance of garnet (grossular) at temperatures below 350 °C is explained by the strong partitioning of CaO into garnet. So that, in rocks with high CaO, garnet may appear at temperatures below 450 °C whereas in rocks with low CaO, garnet may not appear until well above 500 °C (Spear, 1993). Since garnet is stabilized by the incorporation of Ca (that is preferentially fractionated into the first prograde garnet), the first almandine + biotite pair occurs at significantly lower temperatures (Bucher and Grapes, 2011) as low as 480 °C by the following reaction (Winkler, 1979, mineral abbreviations are after Bucher and Grapes (2011)).

$$Chl + Ms + Czo = Alm + Bt + H_2O$$

According to Guidotti et al. (1989), the enrichment of sodium in muscovite and an increase of Mg content in biotite and chlorite (Fe-Penninite is transformed to Penninite) at upper grades is due to the following continuous reaction:

$$Fe\text{-}Chl + Ms = Alm + Mg\text{-}richerBt + Mg\text{-}richerChl +$$

$$Na\text{-}richerMs + H_2O$$
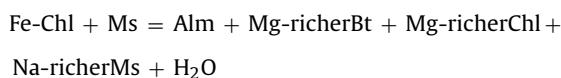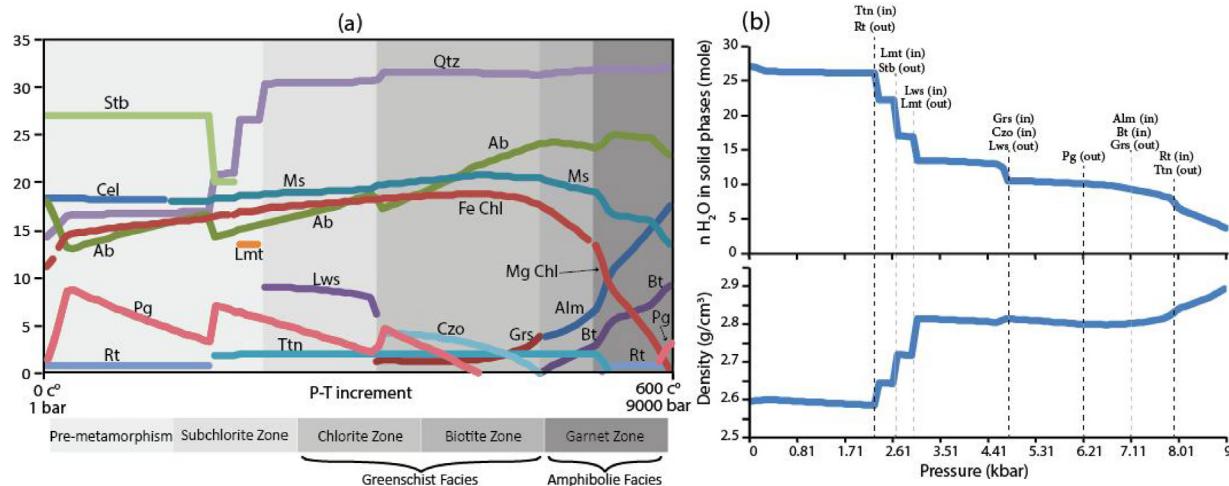
Fig. 14. (a) Predicted mineral evolution for the P-T increment of rutile-bearing garnet schist in the Bajgan Complex calculated using Theriak-Domino (de Capitani and Petrakakis, 2010). **(b)** Calculated water decrease and density increase during the P-T increment, using bulk chemistry of rutile bearing garnet schist.
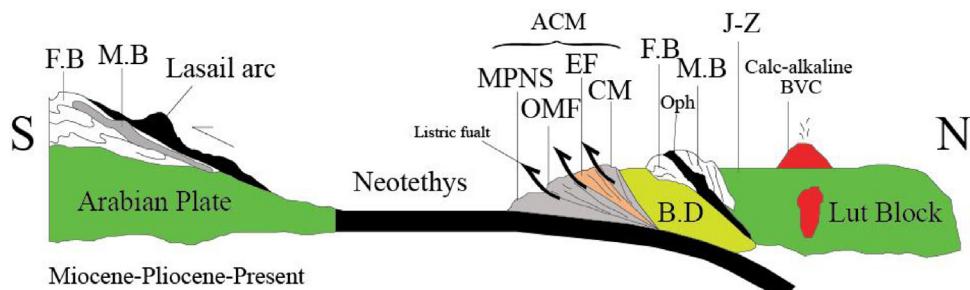
Fig. 15. A cross section through the active subduction zone in the Iranian Makran, at present time (ACM, Active Continental Margin; CM, Coloured Mélange; B.D, Bajgan–Durkan continentalsliver; EF, Eocene Flysch; F.B, Folded Belt (passive margin sediments); J-Z, Jaz Murian depression; OMF, Oligo-Miocene Flysch;M.B, Metamorphic Belt; Oph, Ophiolite remnant; MPNS, Miocene – Pliocene Neritic and Molassic Sediments). (After Omrani et al., 2017; with modification).

The sequence of index minerals from chlorite to garnet is interpreted as zones of progressive metamorphism and implies that rutile-bearing garnet schists experienced greenschist and amphibolite facies metamorphism (Fig. 14a) during collision of Bajgan-Dur Kan microcontinent with and Central Iran.

6.2. Evolution of the Makran and the Bajgan Complex

Fig. 15 shows the cross section of the active subduction zone in the Iranian Makran and geotectonic zones at present time, which consists of the Makran accretionary prisms, coloured mélange complex, Bajgan-Dur kan complex, Band-e-Zeyarat and Dar-e-Anar ophiolitic complexes as well as the Jaz Murian Depression (McCall, 1997; Omrani et al., 2017). The Makran, together with southern and Central Iran and the Zagros, are parts of a Paleozoic microcontinent, which was detached from the edge of Gondwana during Triassic time (McCall, 2002). Presence of the Jurassic pelagic rocks in the Inner Makran, suggests the development of a rift, McCall and Kidd (1982) believe that subductionof the Neotethys between the Arabian, the lower plate external zones to the SW, and the Makran, upper plate internal zones to the NE may have commenced by Middle Jurassic. On the other hand, the inferred subduction was responsible for the volcanic activity in the Inner Makran spreading zone and the occurrence of calc alkaline ophiolites in the inner NE side of the microcontinental slivers of the Bajgan and Dur kan complexes (McCall and Kidd, 1982). K–Ar age for slivers of Bajgan and Dur Kan complexes give an age ranging from 134 ± 4 to 146 ± 5 Ma for low-level gabbros and 121 ± 4 to 130 ± 4 Ma for

high-level gabbros on five hornblende in the Band-e-Zeyarta ophiolite (Hassanipak et al., 1996). This three [40]Ar- [39]Ar plateau ages of 140.7 ± 2.2, 142.9 ± 3.5 and 141.7 ± 1.0 Ma (Ghazi et al., 2004) suggest that these ophiolites formed during the Late Jurassic-Early Cretaceous. The tectonic Coloured Mélange, between the main Makran accretionary prism and the Bajgan/Dur kan Complexes, is a tectonic imbrication of pillow lava, andesites, andesitic tuffs, rhyodacites, welded tuffs, pelagic sediments and exotic components including serpentinite, reefal limestone and amphibolite (McCall and Kidd, 1982; McCall, 2002).

The metamorphic rocks of the Bajgan Complex and the overlying Dur kan Complex are part of a forearc formed on a continental basement and emerged during Cretaceous (McCall and Kidd, 1982). Since the Bajgan Complex is overlain by Carboniferous and Permian limestones of Dur kan to the southeast and Jurassic sediments to the north of the Makran, it must be older than Carboniferous in age (McCall, 2002). Fossil record and K-Ar method suggest that Bajgan Complex age ranges between Paleozoic and Devonian (McCall, 1985a). K-Ar dating of the north extension of this complex indicates a Cretaceous (Senonian) event, which must have been superimposed on the much older complex (McCall, 1985b).

The metapelites of the Bajgan Complex preserve different stages of prograde (Fig. 14a), peak and retrograde metamorphism. The prograde metamorphism which is marked by amphibolite facies may be related to a transition stage from subduction to collision. The absence of HP metamorphism in the metapelitic rocks of the Bajgan Complex shows that the continental margin did not experience metamorphism in the subduction zone. Subduction process continued by initiation of, collision between Bajgan-Dur Kan micro-

continent with and Central Iran and changed the thermodynamic conditions from subduction (cold geotherm) to collision (warm geotherm).

Garnet (Grs) formation began at greenschist facies condition and remained stable as Alm in the amphibolite facies. The late (retrograde) greenschist facies condition is documented by chlorite and clinozoisite that emplaced garnet in the fractures.

Pressure and temperature of about 9 kbar and 600 °C were estimated for the metamorphic peak conditions which correspond with a depth of ~30 km and analogous to Barrovian metamorphism. The textural and petrographic evidence and the estimated conditions during prograde and retrograde metamorphism indicate a clockwise P–T path.

Acknowledgements

References

Aghanabati, A., 1995. Geology of Iran. In: Geological Survey of Iran., pp. 606.

Ahmad, T., Posht Kuhi, M., 1993. Geochemistry and petrogenesis of Urumiah–Dokhtar volcanic belt around Nain and Rafsanjan Area; A Preliminary Study: Treatise on the Geology of Iran. Iranian Ministry of Mines and Metals.

Alavi, M., 2004. Regional stratigraphy of the Zagros folded-thrust belt of Iran and its proforeland evolution. Am. J. Sci. 304, 1–20.

Armbuster, T., Bonazzi, P., Akasaka, M., Bermanex, V., Chopin, C., Giere, R., Heuss-Assbichler, S., Liebscher, A., Menchettic, S., Pan, Y., Pasero, M., 2006. Recommended nomenclature of epidote-group minerals. Eur. J. Mineral. 18, 551–567.

Arvin, M., Houseinipour, A., Babaei, A.A., Babaie, H.A., 2001. Geochemistry and tectonic significance of basalts in the Dare–Anar complex: evidence from the Kahnuj ophiolitic complex, southeastern Iran. J. Sci. Islamic Repub. Iran 12, 157–170.

Arvin, M., Babaei, A., Ghadami, G., Dargahi, S., Ardekani, A.S., 2005. The origin of the Kahnuj ophiolitic complex, SE of Iran: constraints from whole rock and mineral chemistry of the Bande–Zeyarat gabbroic complex. Ofioliti 30 (1), 1–14.

Barker, A.J., 1998. Introduction to Metamorphic Textures and Microstructures, second edition. Blackie, Glasgow, pp. 263.

Berberian, M., Alavi-Tehrani, M., 1977. Structural analysis of the Hamadan metamorphic tectonites; a paleotectonic discussion. In: Berberian, M. (Ed.), Contribution to the Seismotectonics of Iran, Part III, 40. Geological Mineralogy Survey of Iran, pp. 263–280.

Berberian, F., Berberian, M., 1981. Tectono-plutonic episodes in Iran. In: Gupta, H.K., Delany, F.M. (Eds.), Zagros-Hindu Kush-Himalaya Geodynamic Evolution, 3. American Geophysics Union, Geodynamics Series, pp. 5–32.

Berberian, M., King, G.C.P., 1981. Towards a paleogeography and tectonic evolution of Iran. Can. J. Earth Sci. 18, 210–265.

Berberian, F., Muir, I.D., Pankhurst, R.J., Berberian, M., 1982. Late Cretaceous and early Miocene Andean type plutonic activity in northern Makran and central Iran. J. Geol. Soc. London 139, 605–614.

Berberian, M., 1976. On the Metamorphic Rocks of the Makuquadrangle; First Documented Evidence of Syntectonic Metamorphism of the Caledonian Movements in Iran. Geological Survey of Iran, Internal Report, 3p.

Berberian, M., 1977. Three phases of metamorphism in the Hadji–Abad quadrangle (southeastern extremity of the Sanandaj–SirjanZone); A Paleotectonic Discussion. In: Berberian, M. (Ed.), Contribution to the Seismotectonics of Iran, Part III, 40. Geological Mineralogy Survey of Iran, pp. 239–262.

Berberian, M., 1983. Generalized tectonic map of Iran (contribution to the Seismotectonics of Iran, Part IV). 1:1,500,000. Geological Survey of Iran, pp. 52.

Berberian, M., 1989. Tectonic evolution of the Iranian mountain belts. 28th International Geological Congress, 1., pp. 129–130, Washington, DC, July 9–19, Abstract.

Berberian, M., 2014. Active tectonics and geologic setting of the iranian plateau. Dev. Earth Surf. Processes 17, 151–171.

Berman, R.G., 1988. Internally-consistent thermodynamic data for minerals in the system Na2O-K2O-CaO-MgO-FeO-Fe2O3- Al2O3-SiO2-TiO2-H2O-CO2. J. Petrol. 29, 445–522.

Bhattacharya, A., Mohanty, L., Maji, A., Sen, S.K., Raith, M., 1992. Non-ideal mixing in the phlogopite-annite binary; constraints from experimental data on Mg-Fe partitioning and a reformulation of the biotite-garnet thermometer. Contrib. Mineral. Petrol. 111, 87–93.

Bucher, K., Grapes, R., 2011. Petrogenesis of Metamorphic Rocks, 8th edition. Springer, Heidelberg Dordrecht London New York, pp. 428.

Byrne, D.E., Sykes, L.R., Davis, D.M., 1992. Great thrust earthquakes and aseismic slip along the palte boundary of the Makran subduction zone. J. Geophys. Res. 97, 449–478.

Cathalineau, M., 1988. Cation site occupancy in chlorite and illite as a function of temperature. Contrib. Mineral. Petrol. 23, 471–485.

Cetinkaplan, M., Amaury, P., Osman, C., Koralay, O.E., 2014. P-T-t evolution of eclogite/blueschist facies metamorphism in Alanya Massif; time and space relations with HP event in Bitlis Massif, Turkey. Int. J. Earth Sci. 105, 247–281.

Dasgupta, S., Sengupta, P., Guha, D., Fukuka, M., 1991. A refined garnetbiotite Fe-Mg exchange eothermometer and its application in amphibolites and granulites. Contrib. Mineral. Petrol. 109, 130–137.

Davoudzadeh, M., Lensch, G., Weber-Difenbach, K., 1986. Contribution to the Paleogeography: stratigraphy and tectonics of the Infracambrian and lower Paleozoic of Iran. NeuesJahrb. Neues Jahrb. Geol. Paläontol. 172, 245–269.

de Capitani, C., Petrakakis, K., 2010. The computation of equilibrium assemblage diagrams with Theriak/Domino software. Am. Mineral. 95, 1006–1016.

Deer, W.A., Howie, R.A., Zussman, J., 1991. An Introduction to the Rock Forming Minerals. John Wiley and Sons, New York, pp. 528.

Ernest, W.G., Liu, J., 1998. Experimental phase-equilibrium study of Al- and Ti-contents of calcic amphibole in MORB-A semiquantitative thermobarometer. Am. Mineral. 83, 952–969.

Förster, H., Fesefeldt, K., Kürsten, M., 1972. Magmatic and orogenic evolution of the central Iranian volcanic belt. In: Armstrong, J.E., Hedberg, H.D. (Eds.), 24th International Geologic Congress. Montreal, Québec, Canada, pp. 198–210.

Ghasemi, H., Juteau, T., Bellon, H., Sabzehei, M., Whitechurch, H., Ricou, L.E., 2002. The mafic ultramafic complex of Sikhoran (central Iran); a polygenetic ophiolite complex. CR Geosci. 334, 431–438.

Ghazi, A.M., Hassanipak, A.A., Mahoney, J.J., Duncan, R.A., 2004. Geochemical characteristics, 40Ar-39Ar ages and original tectonic setting of the Band-e-Zeyarat/Dar Anar ophiolite, Makran accretionary prism, S.E. Iran. Tectonophysics 393, 175–196.

Guidotti, C.V., Sassi, F.P., Blencoe, J.G., 1989. Compositional controls on the a and b cell dimensions of 2m1 muscovite. Eur. J. Mineral. 1, 71–84.

Harms, J.C., Cappel, H.N., Francis, D.C., 1984. The Makran coast of Pakistan; its stratigraphy and hydrocarbon potential. In: Haq, B.U., Milliman, J.D. (Eds.), Marine Geology and Oceanography of the Arabian Sea and Coastal Pakistan. Van Nosrand Reinhold Company, New York, pp. 3–26.

Hassanipak, A.A., Ghazi, A.M., Wampler, M., 1996. Rare earth element characteristics and K–Ar ages of the Band-e- Ziarat ophiolite complex, southeastern Iran. Can. J. Earth Sci. 33, 1534–1542.

Hawthorne, F.C., Roberta Oberti Harlow, G.E., Maresch, W.V., Martin, R.F., Schumacher, J., Welch, M., 2012. Nomenclature of the amphibole supergroup. Am. Mineral. 97, 2031–2048.

Haynes, S.J., Reynolds, P.H., 1980. Early development of Tethys and Jurassic ophiolite displacement. Nature 283, 561–563.

Hey, M.H., 1954. A new review of the chlorites. Mineral. Mag. 30, 277–292.

Hodges, K.V., Spear, F.S., 1982. Geothermometry, geobarometry and the Al2SiO5 triple point at Mt. Moosilauke, New Hampshire. Am. Mineral. 67, 1118–1134.

Holdaway, M.J., Lee, S.M., 1977. Fe-Mg cordierite stability in high-grade politic rocks based on experimental, theoretical and natural observations. Contrib. Mineral. Petrol. 116, 443–447.

Hosseini-Barzi, M., Talbot, C.K., 2003. A tectonic pulse in the Makran accretionary prism recorded in Iranian coastal sediments. J. Geol. Soc. London 160, 903–910.

Hunziker, D., Burg, J.P., Bouilhol, P., Quadt, A., 2015. Jurassic rifting at the Eurasian Tethys margin: geochemical and geochronological constraints from granitoids of North Makran, SE Iran. Tectonics 34 (3), 571–593.

Itaya, T., Fujino, M., 1999. K-Ar age- chemistry- fabric relations of phengite from the Sanbagaw a high-pressure schists, Japan. The Island Arc 8, 523–536.

Jacob, K.H., Quittmeyer, R.L., 1979. The Makran region of Pakistan and Iran; trench-arc system with active plate subduction. In: Farah, A., DeJong, K.A. (Eds.), Geodynamics of Pakistan. Geological Survey of Pakistan, Quetta, pp. 305–317.

Jung, D., Küsten, M., Tarkian, M., 1976. Post-Mesozoic volcanism in Iran and its relation to the subduction of the Afro-Arabian under the Eurasian plate. In: Pilger, A., Rosler, A. (Eds.), Afar Between Continental and Oceanic Rifting. E. Schweizerbart'sche Verlag sbuchhandlung, Stuttgart, pp. 175–181.

Kananian, A., Juteau, T., Bellon, H., Darvishzadeh, A., Sabzehi, M., Whitechurch, H., Ricou, L., 2001. The ophiolite massif of Kahnuj (western Makran, southern Iran); new geological and geochronological data. Earth Planet. Sci. Lett. 332, 543–552.

Kawai, T., Windley, B.F., Shibuya, T., Omori, S., Sawaki, Y., Maruyama, S., 2008. Large P-T gap between Ballantrae blueschist/gar net pyroxenite and surrounding ophiolite, southern Scotland, UK; Diapiric exhumation of a Caledonian serpentinite mélange. Lithos 104, 337–354.

Kopp, C., Fruehnb, J., Flueha, E.R., Reichert, C., Kukowski, N., Bialas, J., Klaeschena, D., 2000. Structure of the Makran subduction zone from wide-angle and reflection seismic data. Tectonophysics 329, 171–191.

López-Carmona, A., Kusky, T., Santosh, M., Abati, J., 2011. P–T and structural constraints of lawsonite and epidote blueschists from Liberty Creek and Seldovia: tectonic implications for early stages of subduction along the southern Alaska convergent margin. Lithos 121, 100–116.

Laane, J.L., Chen, W.P., 1989. The Makran earthquake of 1883 april 18; a possible analogue tothe puget sound earthquake of 1965. Geophys. J. Int. 98, 1–9.

McCall, G.J.H., Kidd, R.G.W., 1982. The Makran, southeastern Iran; the anatomy of a convergent plate margin active from the Cretaceous to Present. In: Leggett, J.K. (Ed.), Trench-Fore-arc Geology, 10. Geol. Soc., London, pp. 387–397.

McCall, G.J.H., 1985a. Explanatory Text of the Minab Quadrangle Map: 1:250,000, No. J13. Geological Survey of Iran, Tehran, 530 p.

McCall, G.J.H., 1985b. Area Report, East Iran Project, Area No. 1,Geological Survey of Iran, Report No. 57, 634 p.

McCall, G.J.H., 1997. The geotectonic history of the Makran and adjacent areas of southern Iran. J. Asian Earth Sci. 15, 517–531.

McCall, G.J.H., 2002. A Summary of the Geology of the Iranian Makran, 195. Geol. Soc., London, Special Publications, pp. 237–258.

McCall, G.J.H., 2003. A critique of the analogy between Archaean and Phanerozoic tectonics based on regional mapping of the Mesozoic-Cenozoic plate convergent zone in the Makran, Iran. Precambr. Res. 127, 5–17.

Miyashiro, A., 1973. Metamorphism and Metamorphic Belts. G. Allen and Unwin, London, pp. 492.

Miyashita, A., Itaya, T., 2002. K-Ar age and chemistry of phengite from the Sanbagawa schists in the Kanto mountains, Central Japan and their implication for exhumation tectonics. Gondwana. Res. 5, 837–848.

Moazzen, M., Moayyed, M., Modjarrad, M., Darvishi, E., 2004. Azna granitoid as an example of syn-collision S-type granitisation in Sanandaj-Sirjan metamorphic belt Iran. Neues Jahrbuch für Mineralogie. Monatshefte 11, 489–507.

Mohajjel, M., Fergusson, C.L., Sahandi, M.R., 2003. Cretaceous-Tertiary convergence and continental collision, Sanandaj-Sirjan Zone, western Iran. J. Asian Earth Sci. 21, 397–412.

Morgan, K.H., McCall, G.J.H., Huber, H., 1980. Geology Map of Kahnuj, Geology Survey of Iran, No. 7545, scale 1:100,000.

Najafzadeh, A.R., Arvin, M., Pan, Y., Ahmadipour, H., 2008. Podiform chromitites in the sorkhband ultramafic complex, Southern Iran: evidence for ophiolitic chromitite. J. Sci. Islamic Repub. Iran 19 (1), 49–65.

Okamato, K., Maruyama, S., 1999. High-pressure sythesis of lawsonite in the MORB+H2O system. Am. Miner. 84, 362–373.

Omrani, H., Moazzen, M., Oberhänsli, R., Altenberger, U., Lange, M., 2013. The Sabzevar blueschists of the North-Central Iranian micro-continent as remnants of the Neotethys-related oceanic crust subduction. Int. J. Earth Sci. 102, 1491–1512.

Omrani, H., Moazzen, M., Oberhänsli, R., Moslempour, M.E., 2017. Iranshahr blueschist: subduction of the inner Makran oceanic crust. J. Metamorph. Geol. 35, 373–392.

Palvis, T.L., Bruhn, R.L., 1983. Deep-seated flow as a mechanism for the uplift of broad forearc ridges and its role in the exposure of high P/T metamorphic terraces. Tectonics 2, 473–497.

Passchier, C.W., Trouw, R.A.J., 2005. Microtectonics. Springer-Verlag, Berlin Heidelberg, pp. 366.

Perchuk, L.L., Lavrent'eva, I.V., 1983. Experimental investigation of exchange equilibrium in the system cordierite-garnet-biotite. In: Saxena, S.K. (Ed.), Kinetics and Equilibrium in Mineral Reactions. Springer, New York, pp. 199–239.

Platt, J.P., Leggett, J.K., Young, J., Raza, H., Alam, S., 1985. Large-scale underplating in the Makran accretionary prism, southwest Pakistan. Geology 13, 507–511.

Platt, J.P., Leggett, J.K., Alam, S., 1988. Slip vectors and fault mechanics in the Makran accretionary wedge, southwest Pakistan. J. Geophys. Res. 93, 7955–7973.

Ravaut, P., Bayer, R., Hassani, R., Rousset, D., Al Yahya'ey, A., 1997. Structure and evolution of the Northern Oman margin; gravity and seismic constraints over the Zagros-Makran-Oman collision zone. Tectonophysics 279, 253–280.

Ricou, L.E., 1994. Tethys reconstructed; plates, continental fragments and their boundaries since 260 Ma from Central America to Southeastern Asia. Geodin. Acta 7, 169–218.

Sarkarinejad, K., Sarkarineja, d.K., Faghih, A., Grasemann, B., 2008. Transpressional deformations within the sanandaj-Sirjan metamorphic belt (Zagros mountains, Iran). J. Struct. Geol. 30, 818–826.

Sengoř, A.M.C., Altiner, D., Cin, A., Ustomer, T., Hsu, K.J., 1988. The origin and assembly of the Tethyside orogenic collage at the expense of Gondwana land. In: Audley-Charles, M.G., Hallam, A. (Eds.), Gondwana and Tethys, 37. Geol. Soc., pp. 119–181.

Sengoř, A.M.C., 1984. The Cimmeride orogenic system and tectonics of Eurasia. Bull. Geol. Soc. Am. 195, 1–74.

Smart, C.M., Wakabayashi, J., 2009. Hot and deep; rock record of subduction initiation and exhumation of high-temperature, high-pressure metamorphic rocks, Feather River ultramafic belt, California. Lithos 113, 292–305.

Smith, G.L., McNeill, L., Wang, K., He, J., 2013. Thermal structure and mega thrust seismogenic potential of the Makran subduction zone. Geophys. Res. Lett. 40, 1528–1533.

Spear, F.S., 1993. Metamorphic Phase Equilibria and Pressure-Temperature-Time Paths. Mineralogical Society of America, Washington, DC, pp. 799.

Stocklin, J., 1968. Structural history and tectonics of Iran: a review. Am. Assoc. Petr. Geol. 52, 1229–1258.

Takeshita, H., Gouzu, C., Itaya, T., 2004. Chemical features of white micas from the Piemonte calc-schists, western Alps and implications for K-Ar ages of metamorphism. Gondwana Res. 7, 457–466.

Takin, M., 1972. Iranian geology and continental drift in the Middle East. Nature 235, 147–150.

Thompson, A.B., 1976. Mineral reactions in pelitic rocks: II: calculation of some P-T-X (Fe-Mg) phase relations. Am. J. Sci. 276, 401–454.

White, R.S., Louden, K.E., 1982. The Makran continental margin; structure of a thickly sedimented convergent plate boundary. In: Watkins, J.S., Drake, C.L. (Eds.), Studies in Continental Margin Geology, 34. Am. Assoc. Petr. Geol., pp. 499–518.

White, R.S., 1982. Deformation of the Makran accretionary sediment prism in the Gulf of Oman (North-West Indian Ocean). In: Leggett, J.K. (Ed.), Trench-Forearc Geology: Sedimentation and Tectonics on Modern and Ancient Active Plate Margins, 10. J. Geol. Soc., London, pp. 357–372.

Winkler, H.G.F., 1979. Petrogenesis of Metamorphic Rocks. Springer–verlag, New York.